# A Twenty-Year Dynamical Oceanic Climatology: 1994-2013. Part 2: Velocities, Property Transports, Meteorological Variables, Mixing Coefficients

*Draft Version 1.3**

The ECCO Consortium (M. Buckley[8], J.-M. Campin[3], A. Chaudhuri[1], I. Fenty[2], G. Forget[3], I. Fukumori[2], P. Heimbach[3,4], C. Hill[3], C.King[3], X. Liang[5], A. Nguyen,[4] C. Piecuch[1], R. Ponte[1], K. Quinn[1], M. Sonnewald[3], D. Spiegel[3], N. Vinogradova[7], O. Wang[2], C. Wunsch[3,6])†

June 13, 2017

**Abstract**

The World Ocean Circulation Experiment (WOCE) was created to produce the first truly climatologically useful picture of the ocean circulation and its variability. This goal is addressed here from the state estimate of the Estimating the Circulation and Climate of the Ocean (ECCO) consortium, which uses almost all of the data obtained during WOCE and its aftermath along with the much improved general circulation modeling capabilities. A dynamically and data-consistent, state estimate is available depicting the ocean and its ice-cover over a 24-year time-span, globally, from the sea surface to the sea floor. The resulting time-dependent 20-year long climatology includes temperature, salinity, surface elevation, bottom pressure, sea-ice, and three components of velocity. Accompanying the state estimate are modified estimates of meteorological forcing-fields, ocean interior mixing coefficients, and initial conditions. Much spatial structure persists through the two-decade averaging. Results here are primarily pictorial in nature, intended to give the wider community a sense of what is now available and useful and where more detailed analysis would be fruitful. An extended reference list is included.

*For corrections, additions, comments and criticisms please email carl.wunsch@gmail.com.

†1. AER, Inc., 2. Jet Propulsion Laboratory, 3. MIT, 4. U. Texas Austin, 5. U. South Florida, 6. Harvard U., 7. Cambridge Climate Institute, 8. George Mason U.

# 1 Introduction: The State Estimate (Mostly Repeated from Introduction to Part 1)

*Purpose*

One of the central goals of the World Ocean Circulation Experiment (WOCE) was to produce the first truly global time-varying estimate of the circulation over approximately a decade, an estimate that would be useful in defining the major climatologically important ocean elements. The Estimating the Circulation and Climate of the Ocean (ECCO) project was formed near the start of the WOCE field program so as to address this goal using both the conventional and newly-deploying WOCE observation system, along with the rapidly advancing general circulation modelling capability (Stammer et al., 2002). In this paper, and in subsequent Parts, this WOCE goal is addressed by defining a time-dependent climatology over the 20-year (bidecadal) interval 1994-2013. Little or no dynamical or kinematical interpretation is provided—that is left to other authors and times.

Various oceanic climatologies are in use by the oceanographic and climate dynamics communities. They serve as tests of models, as initial conditions, and as a basic descriptor of the ocean. Definitions of climatologies vary widely both in terms of how they were formed and the durations they represent. Here we describe a 20-year average modern climatology from a dynamically consistent model that also has a consistent fit to the majority of global data between 1992 and 2015 (Wunsch and Heimbach, 2013; Fukumori et al., 2017). The climatology is based upon the ECCO version 4 state estimate (Forget et al., 2015). It derives from a least-squares fit of the evolving MITgcm (Marshall et al., 1997; Adcroft et al., 2004; Forget et al., 2015) to the numerous and diverse global observations. A summary would be that all of the Argo, altimetry, the CTD hydrography appearing in the WOCE Climatology and successors (Gouretski and Koltermann, 2004; Talley et al., 2016), all extant, bias error-corrected XBTs, the considerable elephant seal profile data (Roquet et al., 2013), GRACE mission mean and time-dependent geoids, satellite-measured sea surface temperature and salinity, and the ECMWF[1] ERA-interim reanalysis of the meteorological variables (Dee et al., 2011, 2014), have been included, with the fits inferred to be adequate relative to the estimated uncertainties of the data. (Atmospheric reanalyses should not be considered "data", however.)

Previous climatologies, e.g. Levitus et al. (1982) and its later incarnations as the NOAA World Ocean Atlas, or Gouretski and Koltermann (2004) have usually been based only upon temperature and salinity averages and over much longer time intervals than employed here. Other climatologies (e.g., AchutaRao et al., 2007) have focussed on the upper 700 or 1000m

[1] European Centre for Medium Range Weather Forecasts

and relied heavily on XBT measurements. Ishii et al. (2005) is a climatology of the sea surface temperature. As such, all these suffer from the very great inhomogeneities of data distribution prior to the WOCE period and a series of untestable statistical hypotheses (see e.g., Kennedy et al., 2011; Wunsch, 2016; Boyer et al., 2016). This present climatology differs from earlier ones most obviously in its production of the three-dimensional, time-varying, three components of velocity and of a self-consistent surface meteorology, as determined at the model time-step, $\Delta t \approx 1$ h. Use of *any* fluid climatology confronts one basic problem: that the resulting time or space-time average fields do not satisfy any simply derivable equations of motion—requiring a variety of turbulence closure schemes—and the relationships among the different variables can be complicated and poorly known. Here, time/space means of fluid quantities are based upon the uniform average of fields exactly satisfying the model equations at each model time-step (at present, 1 hour) and grid-point. Some authors have used ocean general circulation models fit to data in methods analogous to those in meteorology and commonly known as "reanalyses." These, unfortunately, are usually not property conserving (heat, salt, momentum, etc.) and thus unsuitable for global-scale climate calculations (see e.g., Wunsch and Heimbach, 2013; and Fig. 1 of Stammer et al., 2016).

Some sketches of global-scale analyses of earlier multi-decadal ECCO estimates have been published starting with Stammer et al. (2002). Among them, an earlier 16-year global time-average was described by Wunsch (2011), with a focus on the accuracy of Sverdrup balance, and Wunsch and Heimbach (2014) discussed the heat content changes. Liang et al. (2015, 2017) describe the vertical redistribution of heat and Forget and Ponte (2015) the regional sea level changes. Forget (2010) presented an 18-month estimate from an earlier ECCO state estimate. In general, the present solution differs only subtly from those previously used, with the chief differences being ascribed to the inclusion of more data over a longer duration, inclusion of geothermal heating (see Piecuch et al. 2015), improvements in the handling of sea ice, and where appropriate, separate uncertainties for time-average and time-anomaly measurements. Solutions are generally robust, as much of the volume of ocean in the model state vector is in near-geostrophic balance with the density field at all times longer than a few days.

By choosing the period following 1992, a much more nearly uniform global data coverage is obtained than was possible earlier. Chief among the remaining data inhomogeneities are the intensification of the Argo float profile data availability after about 2005.

Any temporally averaged state will be considerably smoother than states which are sampled more or less as "snapshots." Thus classical ship-borne hydrographic sections (e.g., Fuglister, 1960 or the various WOCE Atlases) show many small-scale features which vanish on averaging. Suppressed features include internal waves, tides, and geostrophically balanced eddy motions.

Meandering currents, such as the off-shore Gulf Stream, are broader and smoother than in any near-synoptic estimate. In addition, fluid regions that are only marginally or poorly resolved numerically (particularly boundary currents), will be smoother than even a true 20-year average would be. Nonetheless, even a 20-year average leaves remarkably many structures much smaller than the basin-scale in the estimated circulation.

No model with a nominal horizontal grid-spacing of $1^\circ$ of longitude can resolve small-scale circulation features, which include the important boundary currents. Nonetheless, the near-geostrophy of the bulk of the ocean supports the conjecture that to the extent that a successful fit to the interior temperature, salinity, and altimetric fields and surface boundary conditions, has been obtained, the boundary currents will be forced by the interior flows to carry the appropriate amount of mass (volume), temperature, etc. so as to satisfy the basic overall conservation laws. This conjecture, upon which we rely, but which is tested elsewhere, can be regarded as a re-statement of that used by Stommel and Arons (1960) in their discussion of deep boundary currents—whose existence and structure was fixed by the mass and property requirements of the interior flow—even though they were not dynamically resolved.

As with any estimation problem, a crucial element in the determination of the best values lies with the use of realistic error estimates for *all* of the data that are being fit. For a full discussion of the error estimate used here, reference must be made to the literature. Temperature measurements are described by Forget and Wunsch (2007) and Abraham et al. (2013). Altimetry accuracies are discussed by Fu and Haines (2013) and Forget and Ponte (2015). For the gravity data from the GRACE mission, see Quinn and Ponte (2008). Satellite surface salinities are addressed by Vinogradova et al. (2014). Meteorological variable accuracies are described e.g., by Chaudhuri et al. (2014, 2016).

This paper is *not* an in-depth analysis of *any* features of the global ocean circulation. It is instead mainly visually descriptive—a suggestive pictorial subsample—intended primarily to serve as an invitation to the wider community to exploit it by demonstrating various products. With the widespread recognition that a steady-state ocean never exists, attention turns instead to the temporal changes over the estimation period. Here for descriptive purposes, a few pictures of changes year-by-year for 20 years, by 20-year averages for each month, and by season, are displayed. All results can readily be calculated month-by-month at the expense of using a larger volume of numbers.

Results here are intended mainly to be indicative of possibilities and an invitation to use, rather than being the most precise or accurate possible. Thus for example, the heat capacity, $c_p$ and the mean density, $\bar{\rho}$ are treated as constant in calculations of heat uptake even though both are (weak) functions of position.

*The State Estimate*

The ECCO state estimate is obtained from the *free-running* MITgcm after the adjustment of the control parameters required to fit the data. In the least-squares methodology with Lagrange multipliers (see Wunsch and Heimbach, 2013), the entire interval 1992-2015 has been fit to the data. Parameters adjusted include the three-dimensional, top-to-bottom, initial conditions, internal mixing coefficients, and the surface meteorology. At any given time in the estimation interval, the solution represents data both preceding and *following* that date so that the equations are always satisfied while coming as close to the data as possible within uncertainty estimates. The 20-year period 1994-2013 has been chosen for averaging as sufficiently distant from the poorly constrained earlier years before the high accuracy altimetry begins in late 1992 and the time of the then non-existent data following 2016. The period corresponds to that of complete coverage by satellite altimetry, the WOCE CTD survey, and the interval after about 2005 when the Argo array became fully-deployed. All data, plus the ECMWF estimate, have been assigned uncertainties that include both instrumental and natural noise. After adjustment of the parameters, the state estimates are the solution to a forward model satisfying all basic conservation requirements. Structurally, it is no different from any other unconstrained model estimate except that its residual data misfits are fully known.

No state estimate is definitive or "correct"; they are "best-estimates" for the present time: data are continuously added, both from more recent years and previously omitted earlier values; estimated data errors are sometimes revised; models are improved; and in all situations, minimizing iterations are ongoing. Values shown here are obtained from ECCO version 4 as of mid-November 2016.

Undoubtedly the state estimate has residual systematic errors at some level, particularly in data-poor regions and times. To some extent, these will be removed when considering only temporal changes in the state over the 20-years and these latter are given some emphasis. Uncertainty estimates remain an amorphous problem: much of the variability in the model represents deterministically evolving elements. Stochastic elements are introduced by weather, some longer-period meteorological variability, and by elements of the initial-conditions best regarded as random. Because the true probability distributions are not known, discussion of estimate uncertainties is postponed to an intended Part 4.

A full description of the many features of the 20-year global ocean circulation requires a book-length publication, if not a library. The strategy here is to sketch the gross hydrographic and circulation features and to do a limited comparison to a few of the special regions (boundary currents, mixed-layer, etc.) to provide some of the flavor of the differences between a moderate-duration, nearly homogeneous, average and both the more common limited-time analyses usually available (classical synoptic hydrographic sections), as well as the far more data-inhomogeneous published climatologies.

With time-mean fields being spatially and temporally smoother than in nominally synoptic measurements, second order quantities such as the time averages e.g., $\langle \mathbf{v} \rangle \langle T \rangle \neq \langle \mathbf{v}T \rangle$, where $\langle \cdot \rangle$ denotes a space-time average, and the difference between them may be very large. Much of physical oceanography has been based upon the unstated assumption that quasi-synoptic measurements represented the mean motion. Thus e.g., the calculation of Sverdrup balance, or of "abyssal recipes", are implicitly steady-state results, despite the common use of individual hydrographic stations or sections. Here true 20-year average estimates are now possible. This description and discussion thus largely focusses on the properties of single variables, $T, u$, etc., their 20-year means and estimates of the deviation from those means. As Part 2, this paper describes the three dimensional Eulerian velocity field and the estimated (that is, adjusted) meteorological forcing. The hydrographic fields and related properties are discussed in Part 1. Most emphasis is placed on the global fields. A number of higher resolution, regional versions, of the state estimate exist (e.g., Gebbie et al., 2006; Mazloff et al., 2010), and a high northern latitude version is forthcoming (An Nguyen, in preparation, 2017), but these estimates are not further discussed here.

All of the ECCO system output described here is available in Matlab® form at: http://mit.ecco-group.org/opendap/diana/h8_i48/contents.html/[2] as 20-year means, 20-separate annual means, 20-year average individual months, and 20-year average seasonal means (DJF, MAM, JJA, SON) on a grid in 50 vertical levels, of thickness plotted in Fig. 1. Many studies are best done in isopycnal-like coordinate systems; but the present description is confined to calculations in geometrical (latitude-longitude-depth) coordinates, with the interpolations to isopycnals postponed (but see Speer and Forget, 2013 for a mode water discussion).

## 2 Eulerian Horizontal Velocities

*Misfits*

As described in Part 1 (ECCO Consortium, 2017), a misfit can be computed between the state estimate and any particular data type. Here, Fig. 3 displays the misfit to some of the TOGA-TAO equatorial current meter array data (Hayes et al., 1991) annual means to the state estimate. Note that in this case, the data were *not* used as constraints on the state estimate, and are thus a completely independent test. At shallower depths (not shown), the consistency between the two estimates is even better.

[2] Or contact Carl Wunsch directly (cwunsch@mit.edu) for data or advice.

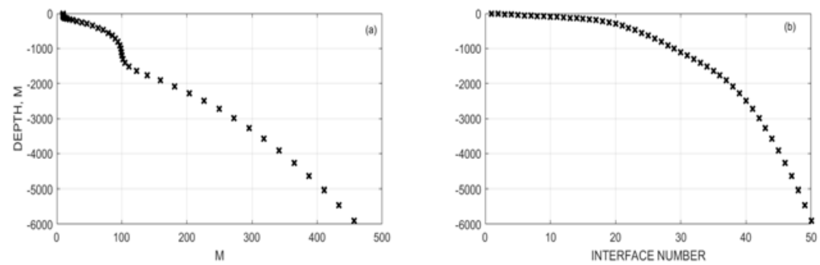


Figure 1: (a) Level thicknesses; (b) level depths in the ECCO version 4 of the MITgcm. {interfaces_la

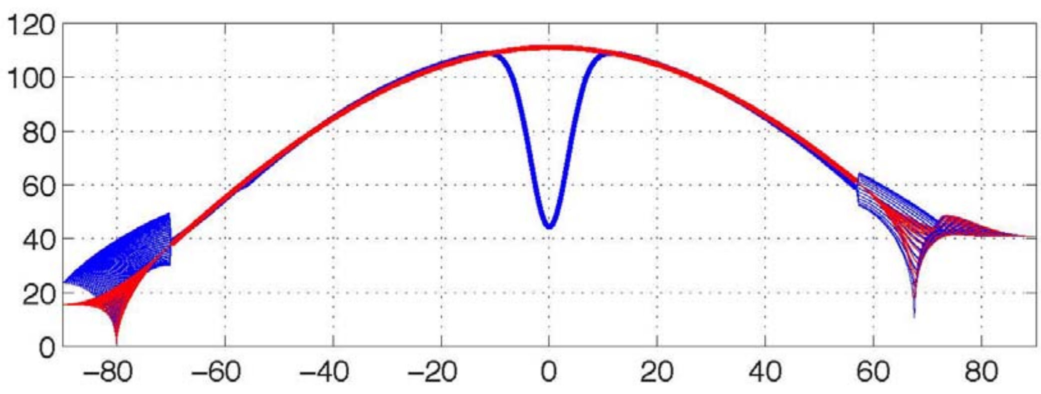

Figure 2: Latitude (blue curve) and longitude spacing in kilometers as a function of latitude (from Forget et al., 2015). Higher latitude spacing exists near the equator. At high latitudes the more complex grid leads to a distribution of spacings (see Figs. 1, 2 of Forget et al., 2015). Most of the high latitude southern region is land. {fig03-eccov4_

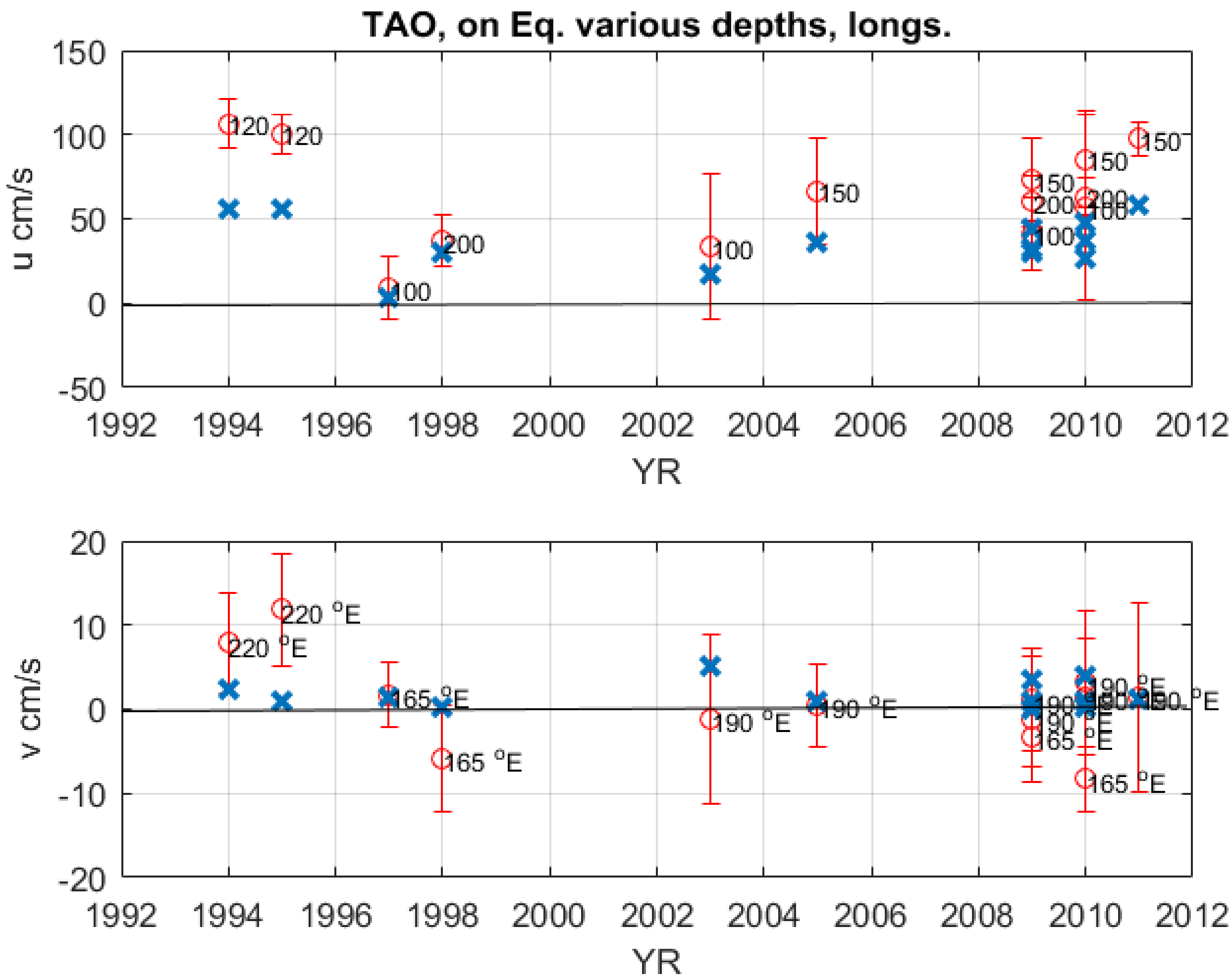


Figure 3: Upper panel shows the $u$ component from the TAO array on the equator at various depths (red symbols) with standard errors. $'\times'$denotes the corresponding ECCO state estimate annual mean. Values are within one standard error. Labels are the water depth. Lower panel shows the same result for the $v$ component. Now the labels indicate the longitude of the measurement. {tao_annmeans_

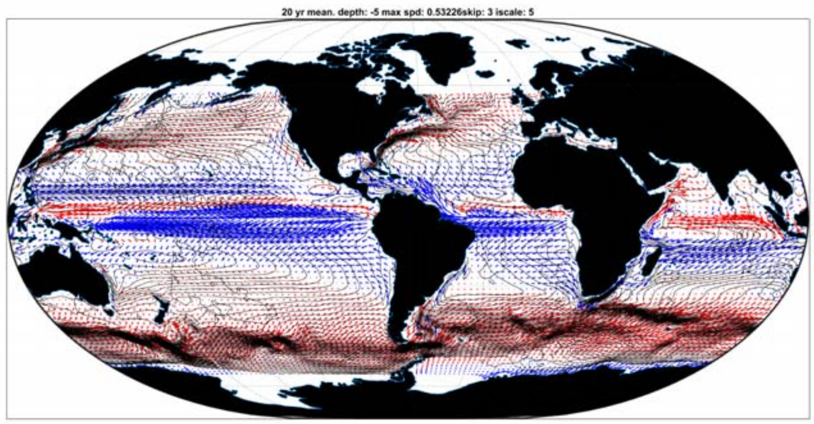


Figure 4: The 20-year average Eulerian flow at 5m depth superimposed upon the time-mean surface elevation, $\eta$. Red arrows have an eastward component, blue a westward one. Largest value here (longest arrow) correspond to 40cm/s. In the centers of gyres, particularly, the ageostrophic component of flow visually crosses the surfaces of constant elevation. {quiver_map_5m

*Time Means*

Figs. 4-8 depict the 20-year Eulerian mean flow fields as arrow plots at four depths. A number of distinct, expected features can be seen. These include the strongly divergent (to north and south) flows on the equator, the western boundary currents and their extensions as well as the Antarctic Circumpolar Current. All of these flows are broader and smoother than is familiar from attempts at instantaneous depictions. The corresponding pressure field contours are also shown as a visual guide.

The time average zonal flow on the equator is displayed in Fig. 9 with a conspicuous equatorial undercurrent; and the average meridional flow across the equator is in Fig. 10. Time average zonal flow in the Drake Passage is shown in Fig. 11 with a net transport of 146Sv, close to most published values (Meredith et al., 2011), but in contrast to the much larger transport claimed by Donohue et al. (2016), the difference probably owing to the strong assumptions made there. The estimated value here is necessarily consistent with the near-geostrophic interior flows both to the west and east of the passage. Mild annual variations in the transport are depicted below. Fig. 12 shows the remarkably complex meridional mean flow at 60°S, a latitude passing through the Drake Passage.

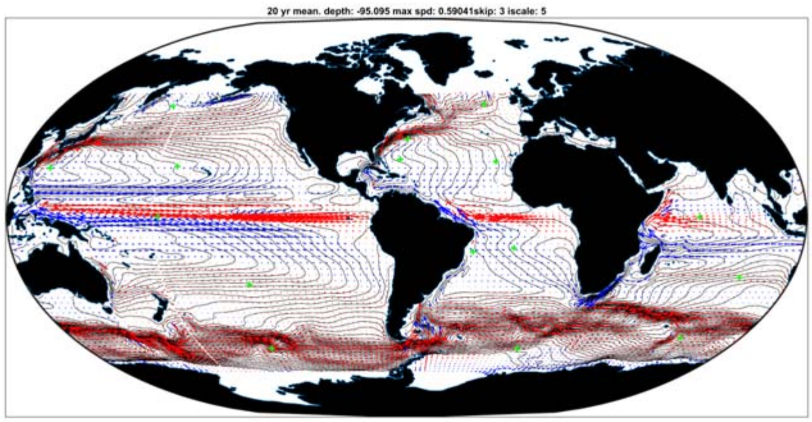


Figure 5: Twenty-year average of the mean horizontal flow at 95m superimposed on the time-mean sea surface elevation. Largest value is 59 cm/s. Vectors more closely follow the elevation lines than does the velocity at 5m in Fig. 4. Note the strong eastward flow on the equator as compared to the near-surface values. {quiver_map_10

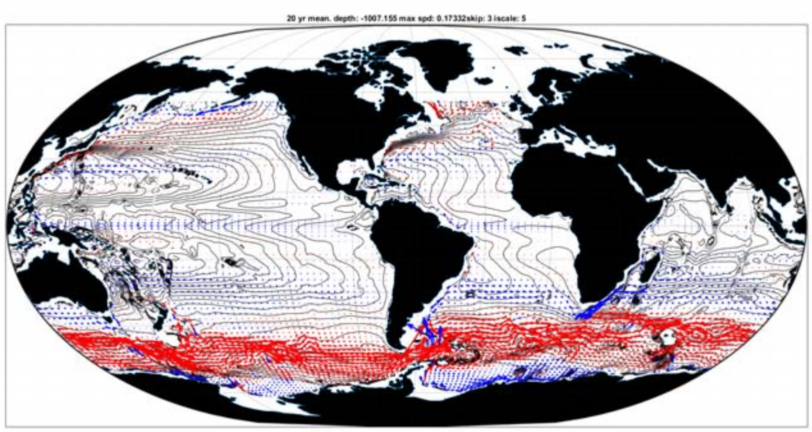


Figure 6: Twenty-year mean flow at 1000m (compare Ollitrault and Colin de Verdiere, 2014). Largest value shown is 17 cm/s, but arrow lengths are saturated in the Southern Ocean. Weak banding is visible in the tropics generally. The corresponding hydrostatic pressure field at this depth is shown. {quiver_map_20

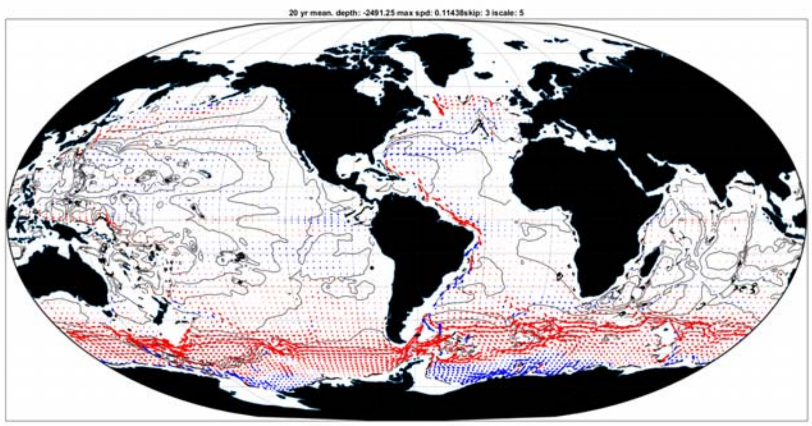


Figure 7: Same as Fig. 4 except at 2500m . Largest arrow corresponds to 13 cm/s. The Atlantic deep western boundary current and the Southern Ocean eastward flow are the most conspicuous features. {quiver_map_20

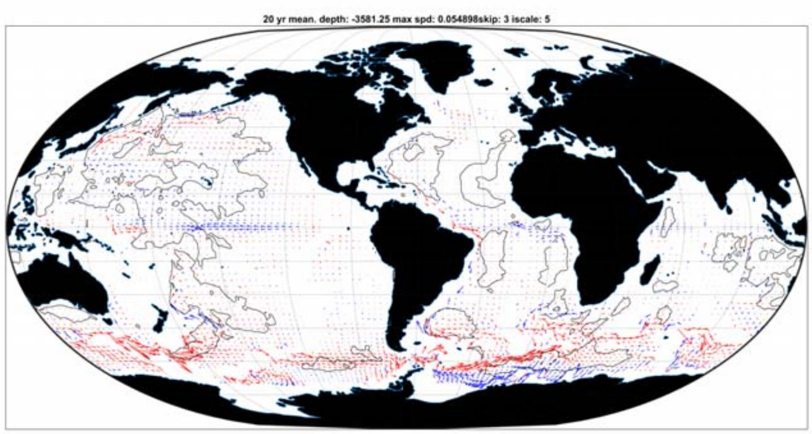


Figure 8: Twenty-year average horizontal flow at 3600m with the 5000m contour and not the pressure field. Largest arrow is 5.5 cm/s. {quiver_map_20

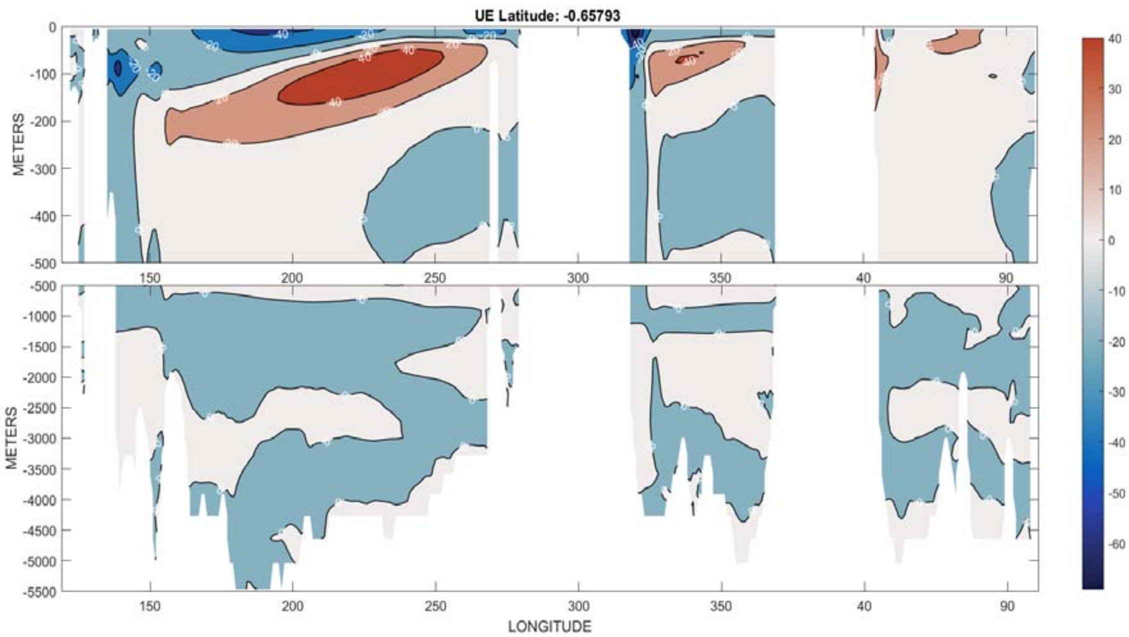


Figure 9: Twenty-year average Eulerian zonal flow, $u$, *along* the equator in all three oceans (cm/s). The eastward flowing equatorial undercurrent is visible in the Pacific and Atlantic Oceans, as is a zonal westward flow below.

{ue_20yr_secti

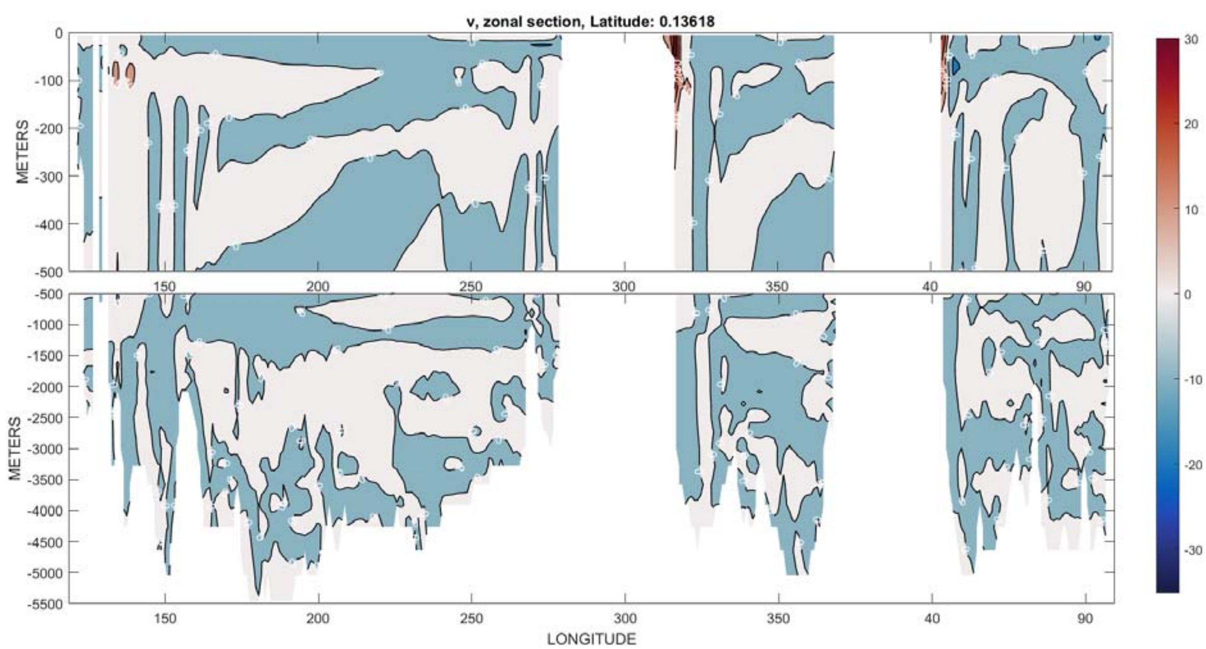


Figure 10: Twenty-year average mean Eulerian meridional velocity, $v$, at the equator (cm/s).

{vn_equatorial

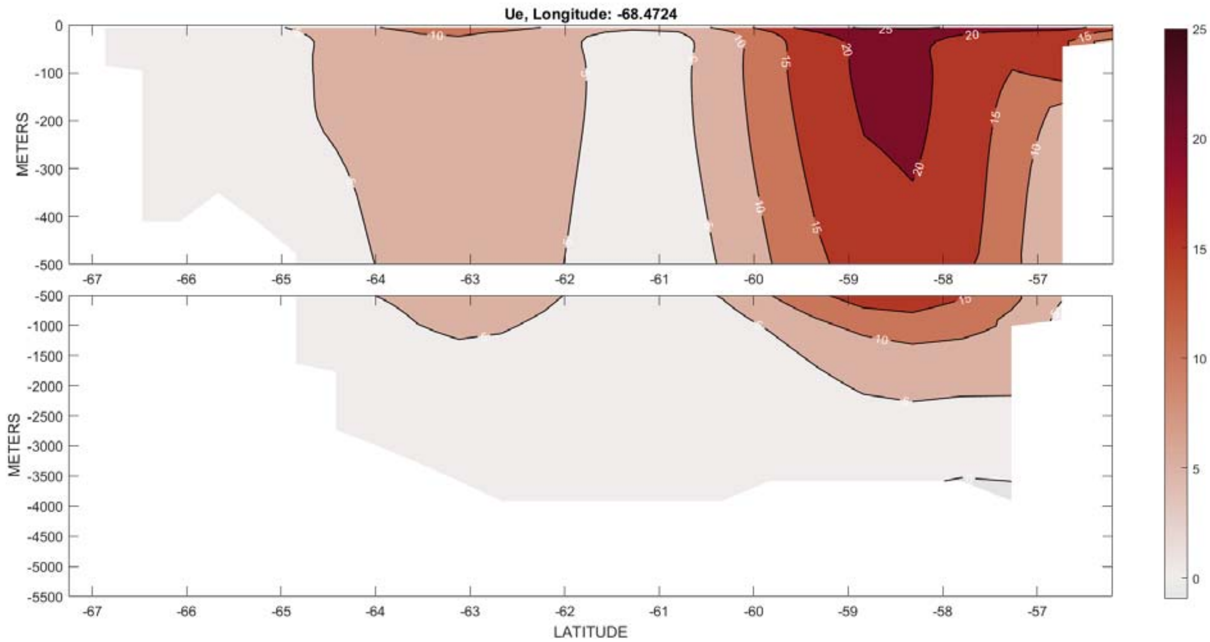


Figure 11: Twenty-year average *zonal* flow, $u$ in the Drake Passage at 70°W. The 20 year average transport is 146 Sv.

{zonalflow_20y

# 3 Time-Dependent Flows

The oceanic flow field varies on all time scales from seconds to the age of the ocean. In Figs. 13-15 are shown the anomalies of Eulerian velocity about the 20-year mean at 5 m.

A few representative anomalies of the annual average meridional component, $v$, are shown in Figs. 16-18 across the equator. Such results become part of the story of tropical variability including the ENSO cycle.

Oceanic kinetic energy is one of its basic physical properties. Fig. 19 displays the logarithm of the 5m depth value of the kinetic energy in one year (2004). As expected, some variation in total kinetic energy (top-to-bottom) for each of the 20 years as well as that for the abyssal layer (3600m to the bottom) can be seen in Fig. 20. The slow overall increase over 20 years and the decay in the abyss are not easily testable.

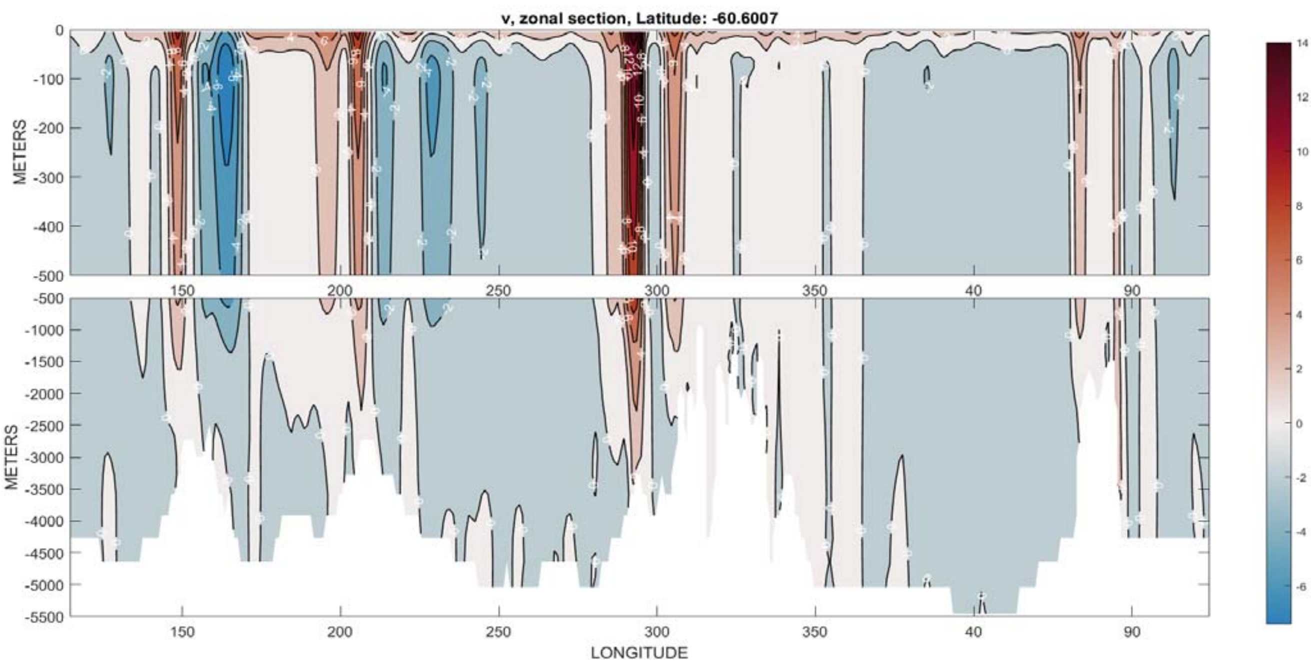


Figure 12: Twenty-year mean meridional velocity, $v$, in a section through the Drake Passage. A conspicuously variable structure survives 20-years of averaging. {vn_drakepassa

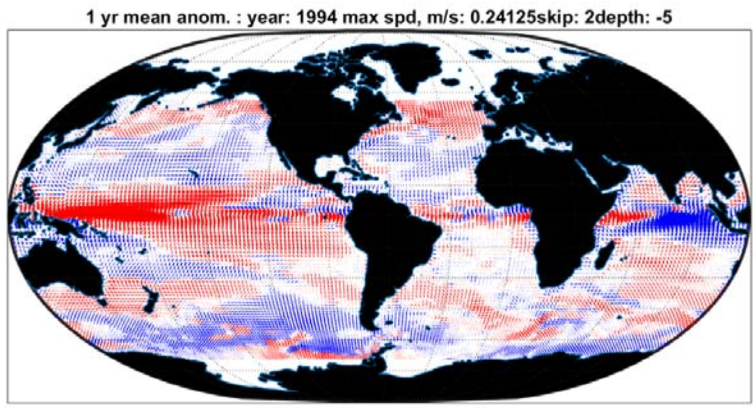


anom yr 1994.tif

Figure 13: Anomaly of the 5m horizontal flow in 1994, again with red arrows having an eastward component. Largest arrow is 24 cm/s. {quiver_anom_y

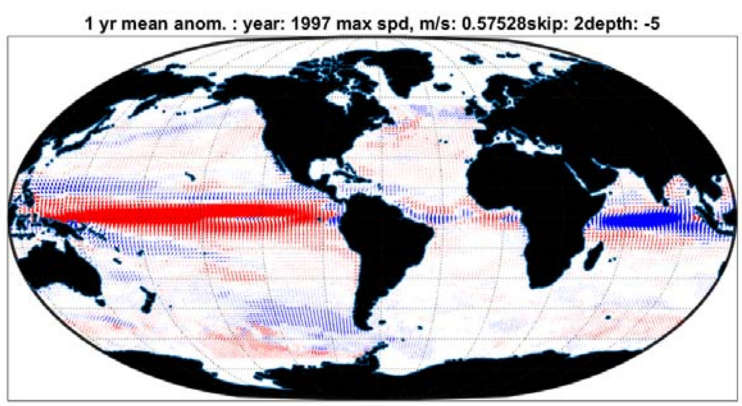


anom yr 1997.tif

Figure 14: Same as Fig. 13 except for 1997 with the largest arrow at 58 cm/s. {quiver_anom_y

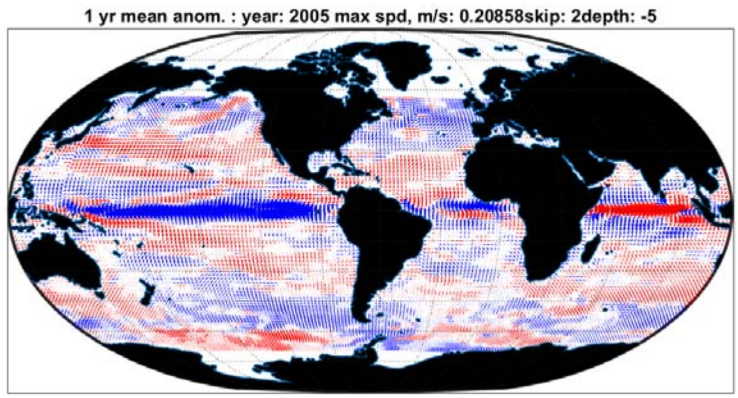


anom yr 2005.tif

Figure 15: Same as Fig. 13 except for 2005 with the largest value be 21 cm/s. {quiver anom y

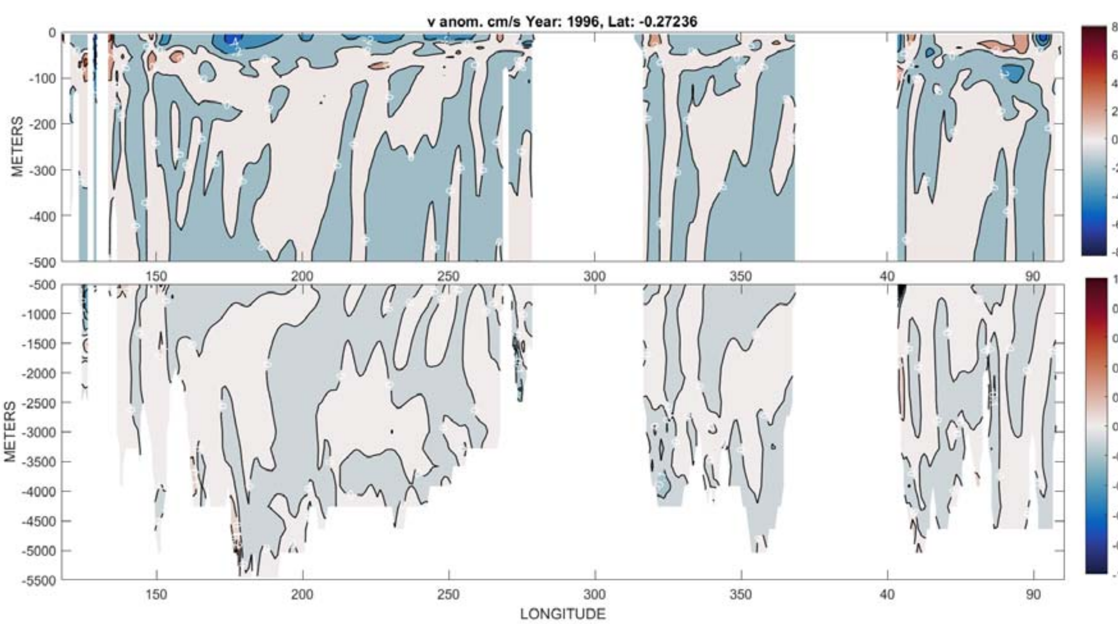


Figure 16: Anomaly of meridional flow across the equator in 1996 (cm/s). {vanom_1996_la

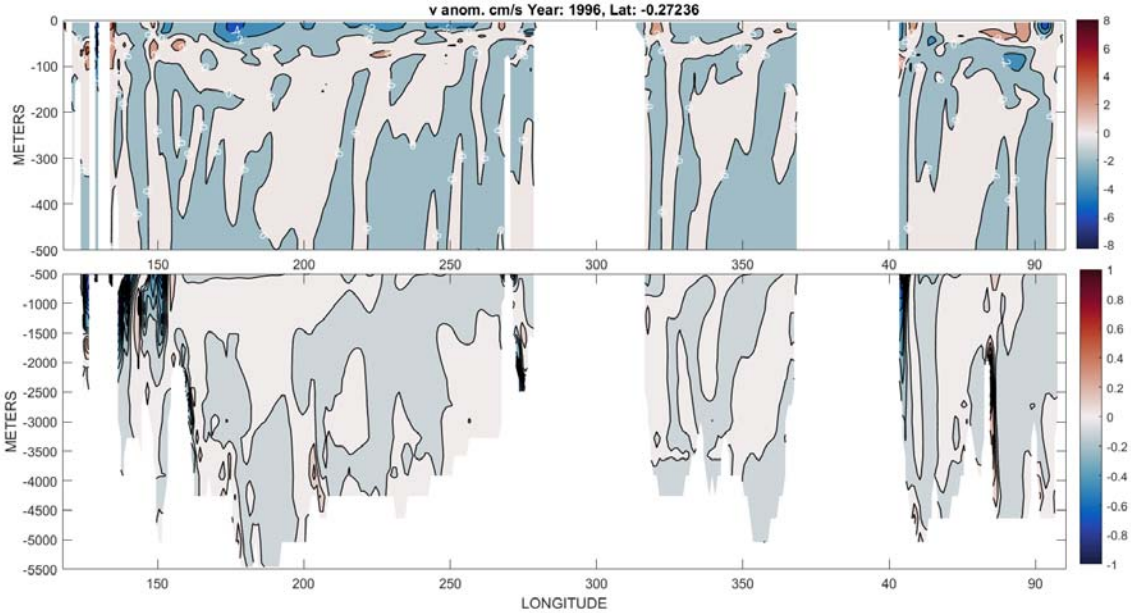


Figure 17: Anomaly of meridional flow across the equator in 1998 (cm/s)—an El Niño year. {vanom_1998_la

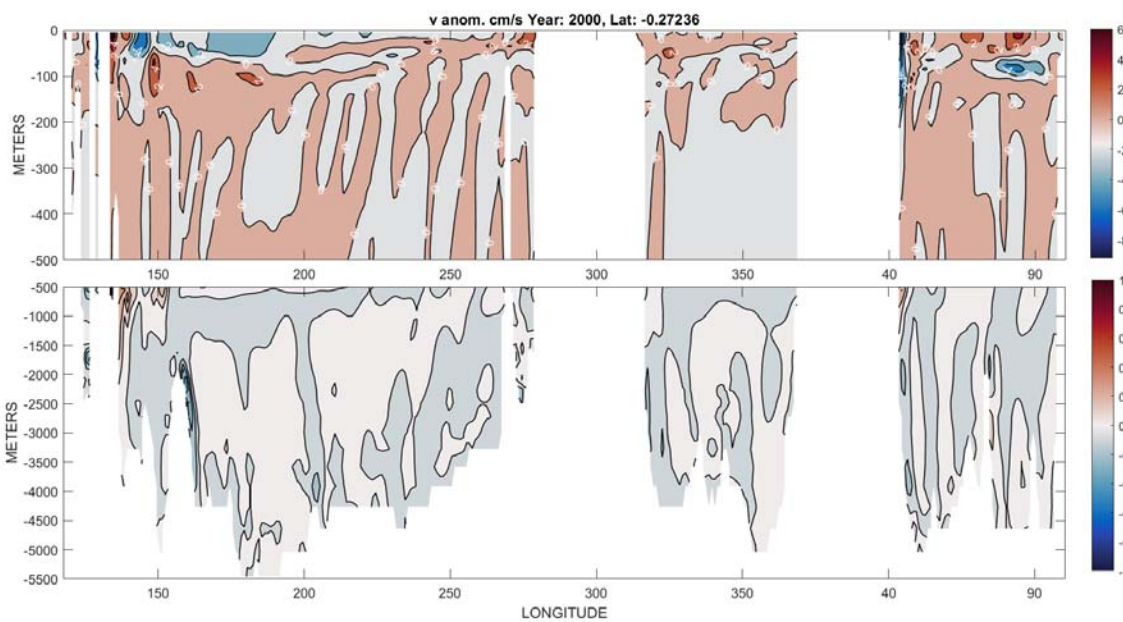


Figure 18: Anomaly of meridional velocity, $v$, (cm/s) at the equator in 2000. {vanom_2000_la

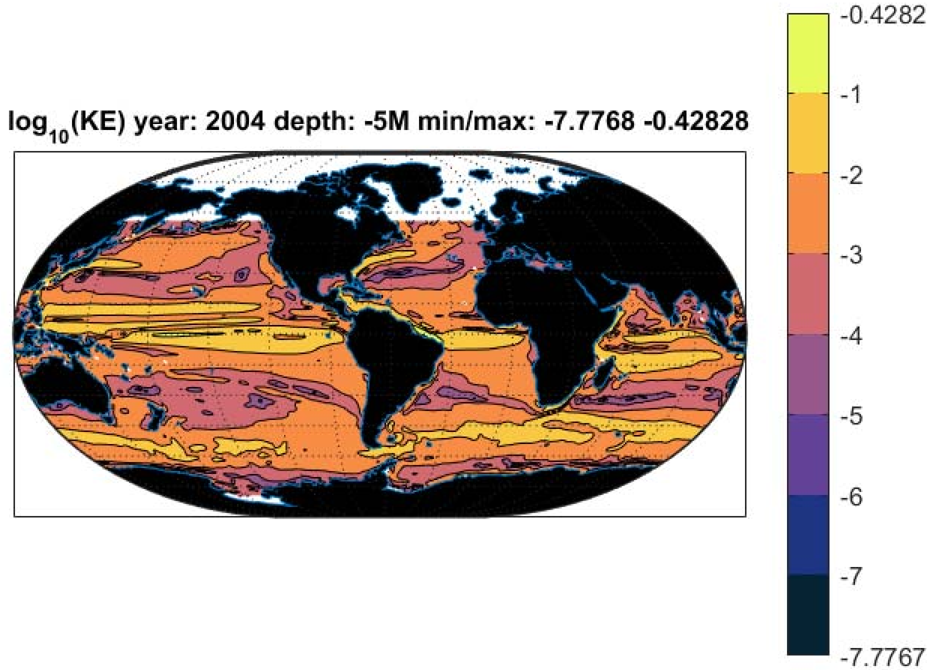


Figure 19: Logarithm of the Eulerian horizontal kinetic energy/unit mass at 5m averaged over 2004. Other years are visually similar, differing in details. {ke_5m_2004.ti

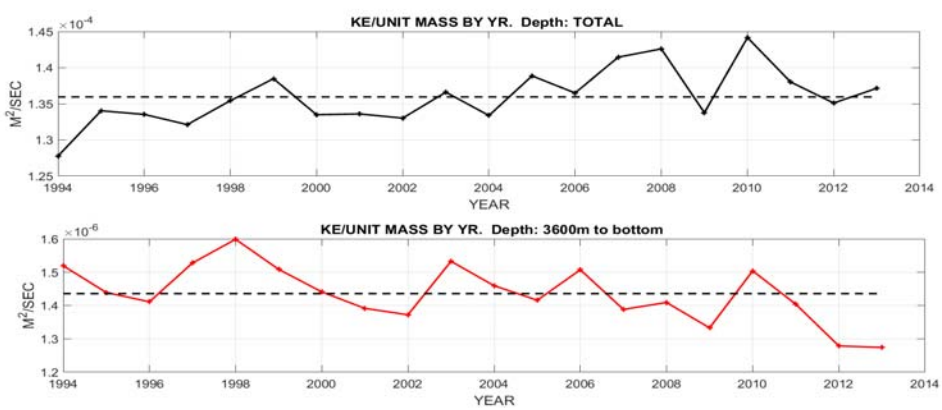


Figure 20: (Upper panel) Total (top-to-bottom) but excluding the northern high latitudes, kinetic energy/kg by year. El Niño year 1998-99 is prominent early in the record. A weak upward trend might be real. (Lower panel) Kinetic energy/unit mass by year in the layer 3600m to the bottom. Note the scale change from the upper panel. {ke_total&3600

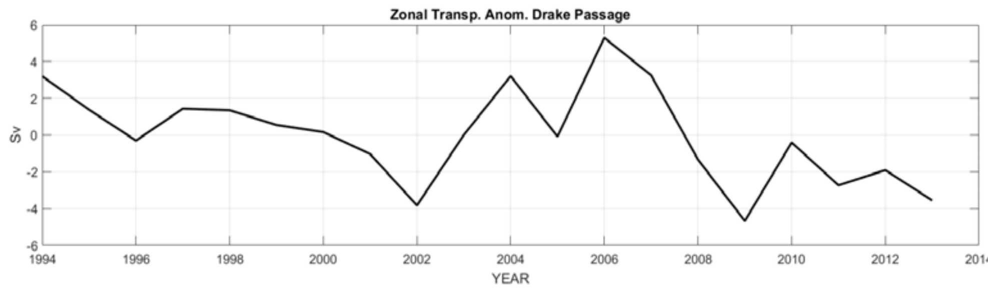


Figure 21: Anomaly (Sv) of transport integrated across the Drake Passage for each year. {yearly_trans_

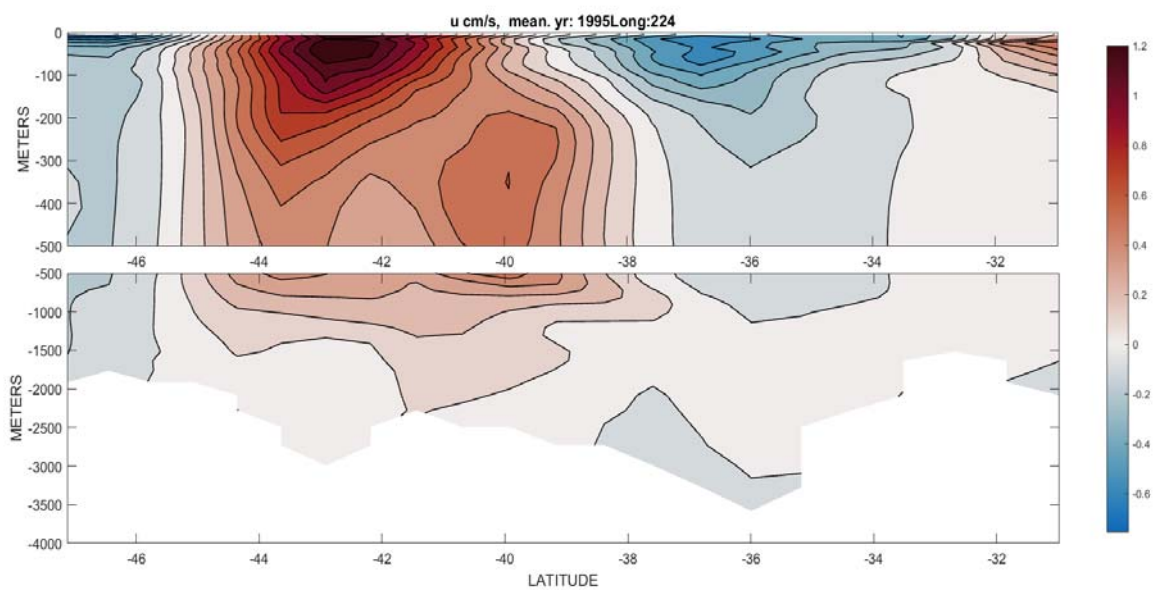


Figure 22: Anomaly of the zonal flow in the Drake Passage in 1995 (cm/s). {u_drakepassag

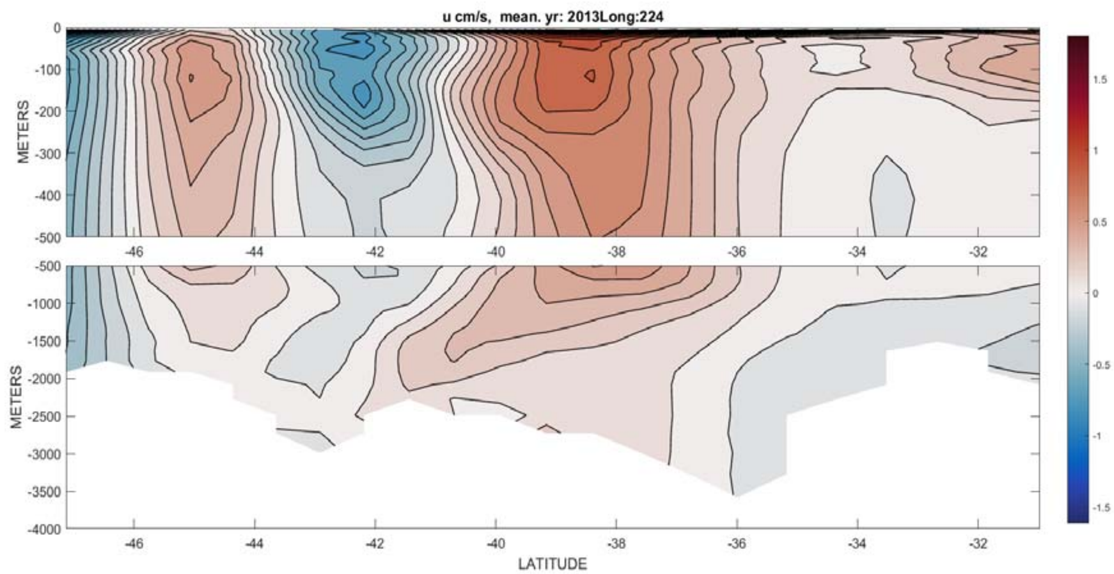


Figure 23: Anomaly of the zonal flow (cm/s) through Drake Passage in 2013. {u_drakepassag

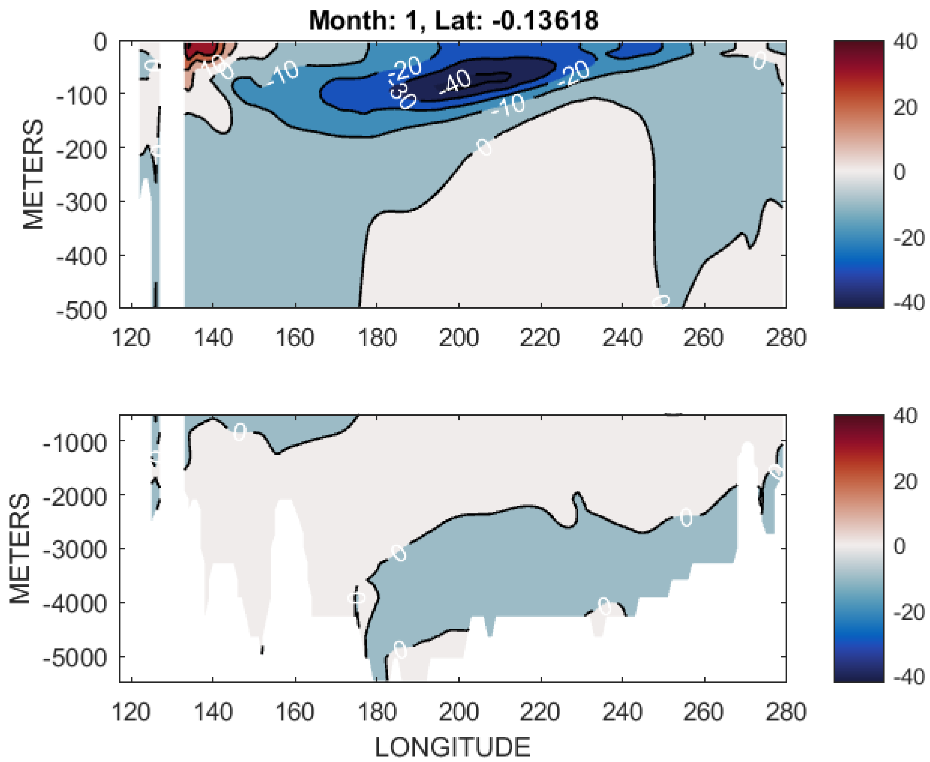


Figure 24: Twenty-year mean zonal flow anomaly (cm/s) on the equator in January in the Pacific Ocean. {equator_jan_s

## 3.1 Annual Cycle

The annual cycle dominates the atmospheric climate system, with a similar strong response in the very upper levels of the ocean. Simple Rossby wave theory (e.g., Gill and Niiler, 1973; Wunsch, 2015) shows that the vertical penetration of the baroclinic response to annual forcing at the surface is very restricted, but a bit deeper on the equator. An example of the mean annual cycle, shown as the 20-year average of the monthly anomaly of $u$, along the equatorial section in the Pacific Ocean is displayed in Figs. 24-27 for a few months.. Although the response in the upper 100 m is far larger than at depth, a detectable annual cycle in $u$ exists to the sea floor. Note that interpretation of the upper ocean structures requires use of the mean flow in Fig. 9, as a positive anomaly will weaken the westward-going near-surface South Equatorial Current, and amplify the eastward moving Undercurrent.

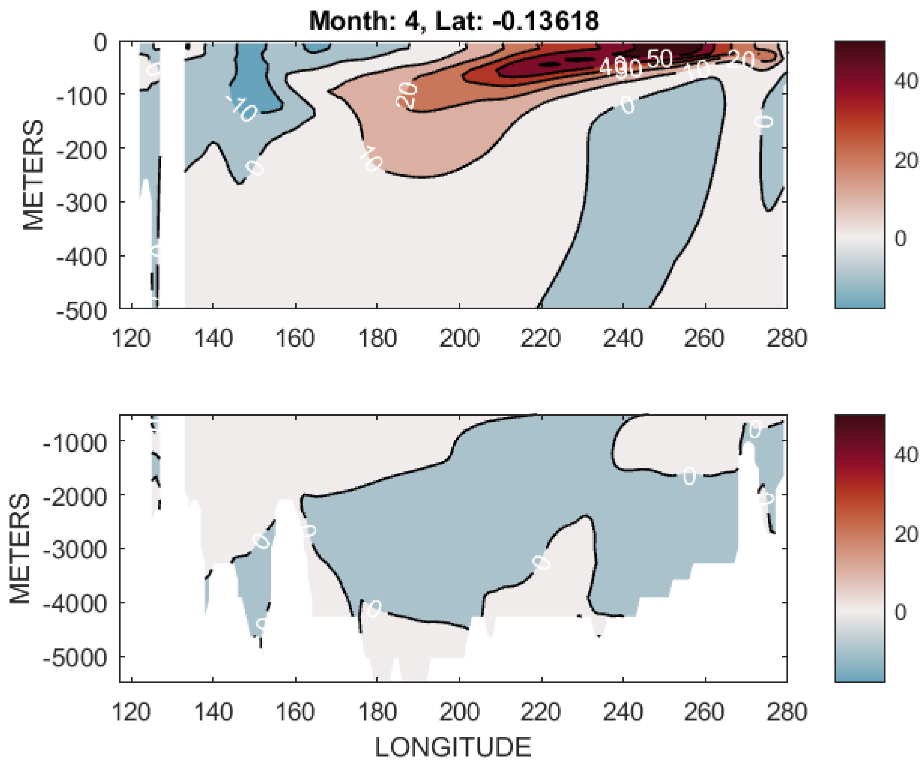


Figure 25: Zonal flow anomaly (cm/s) on the equator, mean April. {equator_apr_s

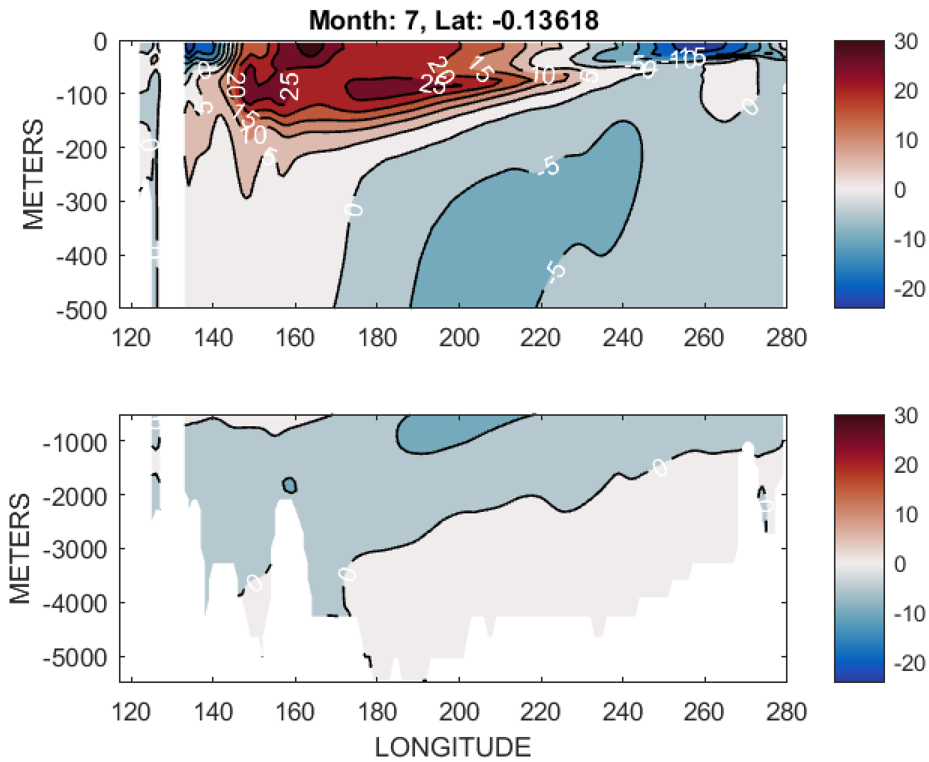


Figure 26: Zonal flow anomaly (cm/s) on the equator, mean July. {equator_jul_s

### 3.2 Meridional Transports

One example of a 20-year time mean flow is shown in Fig. 28 at 30°S in the Pacific Ocean. These are readily computed monthly, seasonally etc. for any location.

When integrated through the entire longitude range of 360°, time-average oceanic mass conservation requires that the top-to-bottom meridional transports must vanish up to the divergence contained in net average evaporation plus runoff minus precipitation. The resulting global mean, accumulating integral is shown in Fig. 29. Residual imbalance, an estimate of the average evaporation minus precipitation appears in Fig. 30, but whose properties will be discussed elsewhere. An earlier result is by Stammer et al. (2004).

### 3.3 Property Transports

The state estimate provides a comprehensive set of output fields on the native grid which permit accurate property transport calculations, consistent with Griffies et al. (2016). As noted already, transport properties involving time mean products such as $\langle vT \rangle$ are expected to be different from values computed from the time means of each, $\langle v \rangle \langle T \rangle$ . Thus Fig. 31 displays the depth,

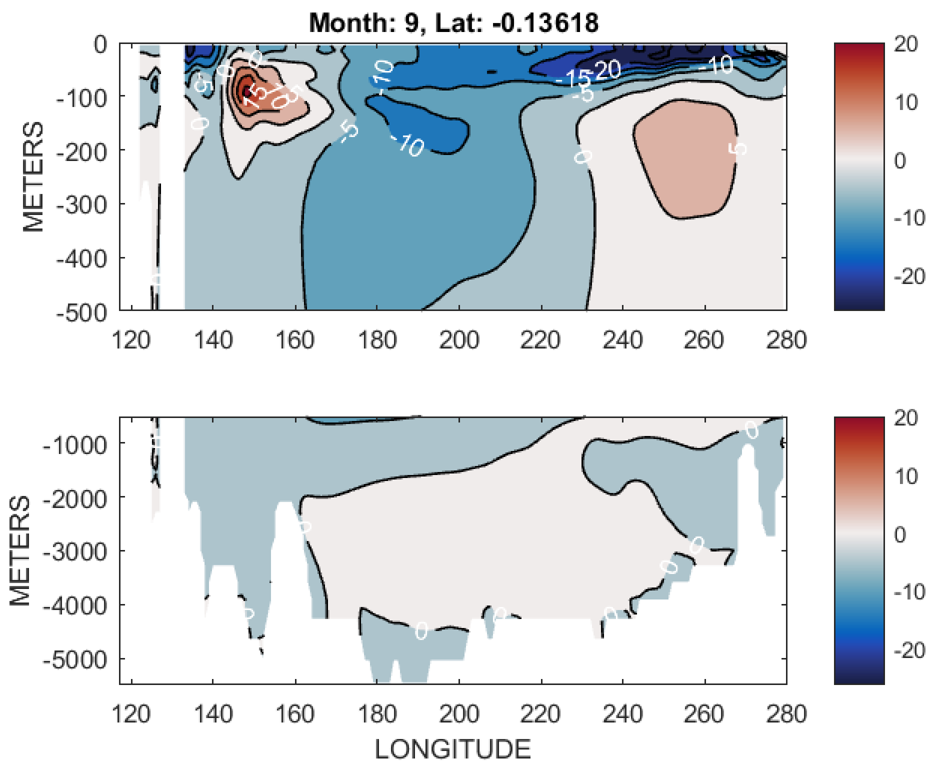


Figure 27: Zonal flow on the equator, mean September. {equator_sep_s

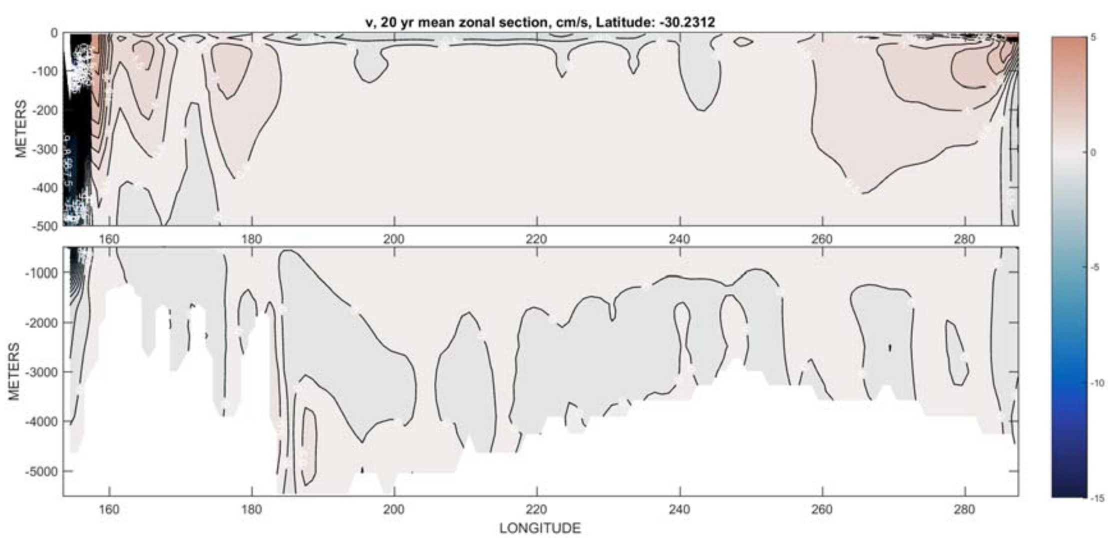


Figure 28: Twenty-year average meridional flow at 30°S in the Pacific Ocean. Intense flow in the East Australia Current and a flow reversing with depth along the coast of South America are visible. As in many such sections, weak deep flow reversals occur throughout. {vn_20yrmean_3

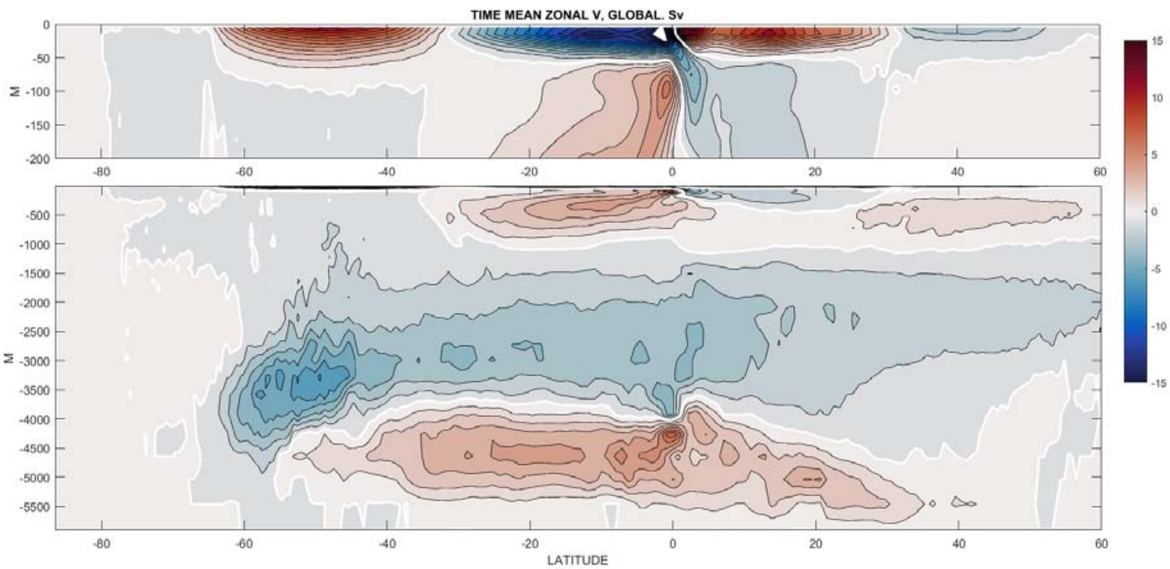


Figure 29: Zonal integral of vertically accumulating meridional transport in Sverdrups. (Not a stream function.) The values at the bottom necessarily almost vanish. See Fig. 30. {zonal_integra

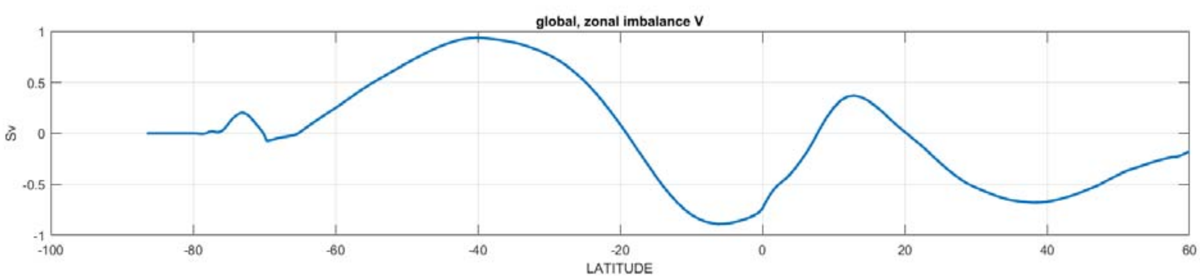


Figure 30: Integral, top-to-bottom, of the meridional transport as a 20-year mean. Bottom value of Fig. 29. Divergence is an estimate of the average evaporation minus precipitation. {global_imbala

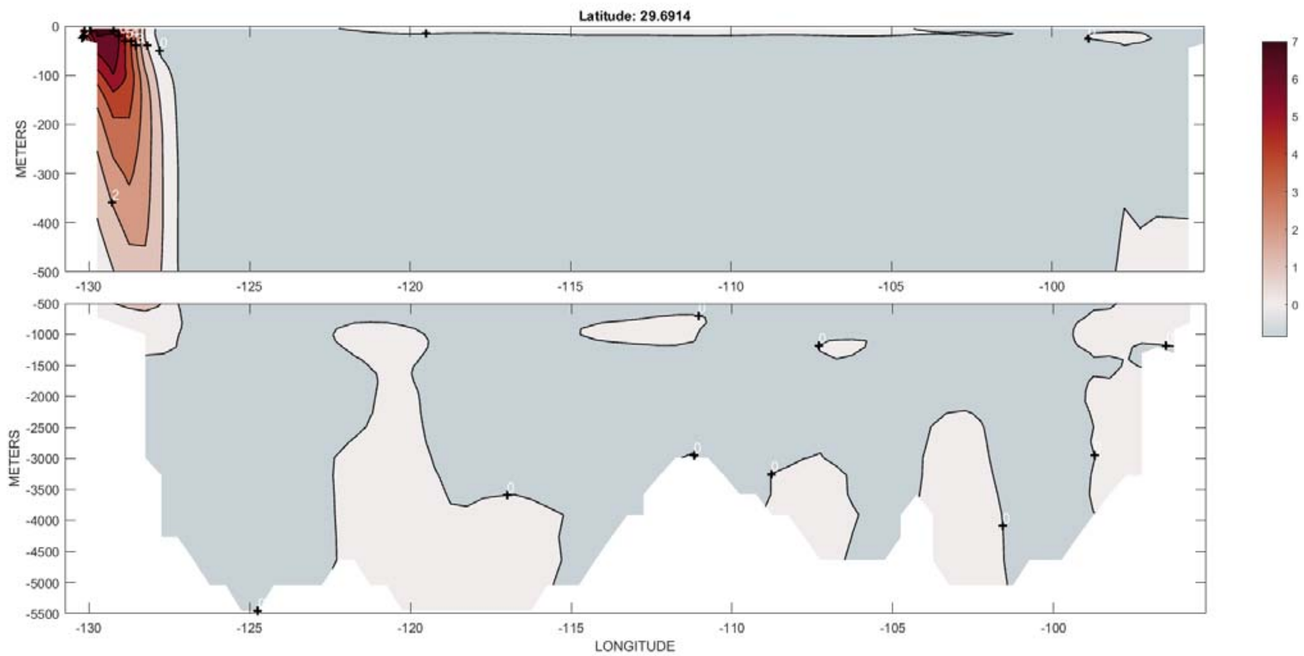


Figure 31: Product of the twenty-year means $\langle \bar{v} \rangle \left\langle \bar{T} \right\rangle$ at 30°N in the North Atlantic (m/s °C) with a reference temperature of 0°C. Corresponding heat transport is 0.6PW in contrast to values computed from quasi-synoptic sections of about 1.3PW (e.g., Bryden and Imawaki, 2003). Southward transport in the weak flowing interior is non-negligible.

{vn_theta_sect

longitude contributions of $\langle v \rangle \langle T \rangle$ 30°N in the North Atlantic, producing an equivalent heat transport of 0.6 PW, smaller than estimates based e.g., on monthly or single section data (e.g., Bryden and Imawaki, 2001; Piecuch and Ponte, 2012, Table 2). As with many of the multi-decadal results, these values are best interpreted as quantitatively descriptive, and as serving as tests of unconstrained results from different models.

The corresponding values in the Pacific Ocean at 30°N are negligible (not shown) with a northward temperature transport mainly in the Kuroshio nearly cancelled by the interior return flow.

# 4 Vertical Velocities

*Eulerian Means*

Vertical velocities in the ocean are almost never measured directly, but must be computed diagnostically from the horizontal flow divergences. The result for the 20-year average at 105m can be seen in Fig. 32 and is a useful surrogate for the Ekman pumping. (See Roquet et al.,

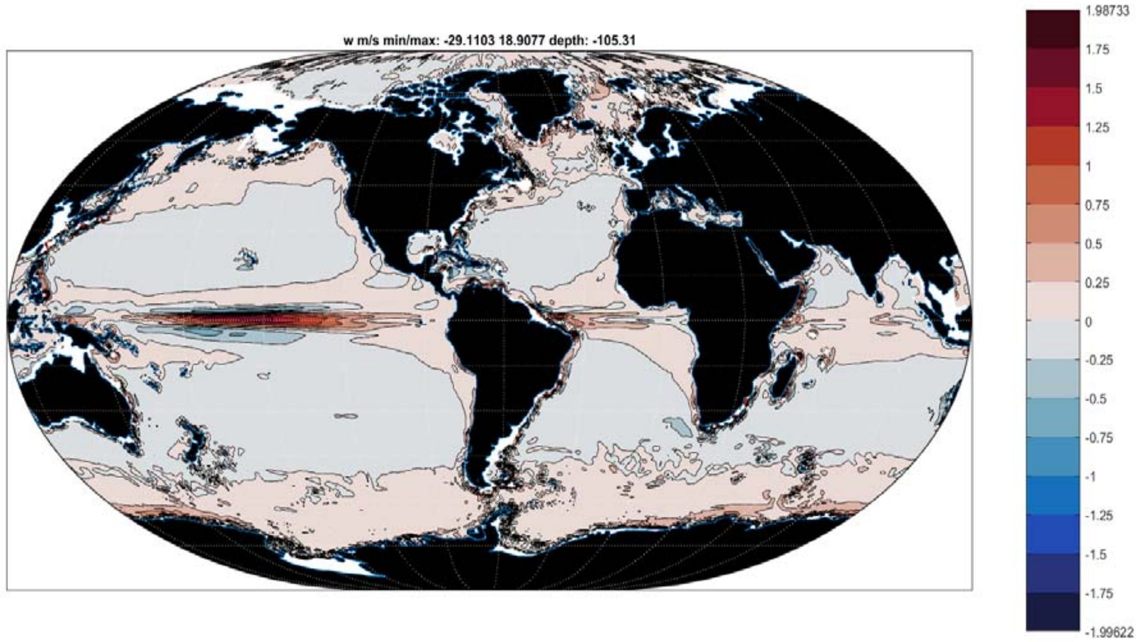


Figure 32: Twenty-year average Eulerian vertical velocity, $w$, (m/s) at 105m depth. Intense upwelling is appparent on the equator in all oceans, at high latitudes, and in traditional coastal upwelling regions. {map_w_105m_20

2011 for an explicit discussion of the latter.) Main features are the subtropical and subpolar gyres as well as the powerful upwelling on the equator and the upwelling zones on the eastern margins. Fig. 33 shows the same result, but at 720m. At greater depths, e.g. 2000m (Fig. 34), the influence of bottom topography has begun to dominate and the complexity of $w$ defies simple description. Liang et al. (2017) provide a fuller discussion.

The mean annual cycle of $w$ at 105m is shown in Figs. 35-38 and can be regarded as a quantitative estimate of the cycle in Ekman pumping.

# 5 Meteorological Variables

Meteorological forcing at the sea surface is part of the state estimate control vector—that is, the a priori windstress, surface air temperatures, specific humidity, shortwave downwelling radiation, and precipitation are modified along with other elements of the control vector so that the model is as consistent as possible with the oceanographic data. Comparatively small adjustments are made to the values obtained from the Dee et al. (2014) ERA-Interim atmospheric "reanalysis."

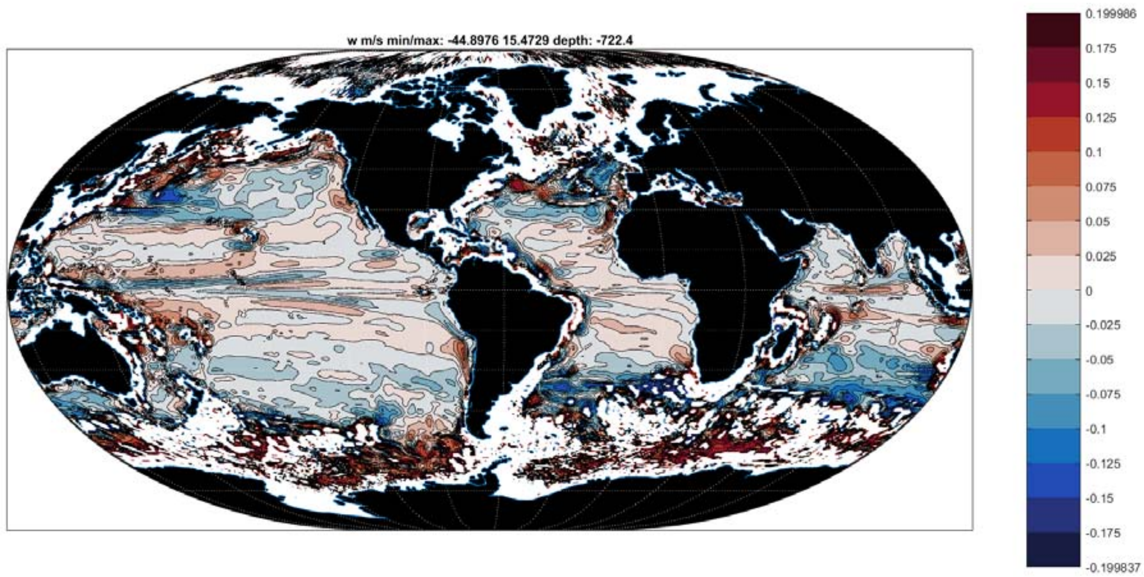


Figure 33: Twenty-year average vertical velocity, $w$, ($10^5$m/s) at 720m. The most conspicuous mid-latitude feature is the zonal banding, with a small residual of the large-scale surface gyres still visible. The Southern Ocean stands out as a region of extremely intense values of $w$ of both signs (extreme values have been truncated there). {map_w_720m_20

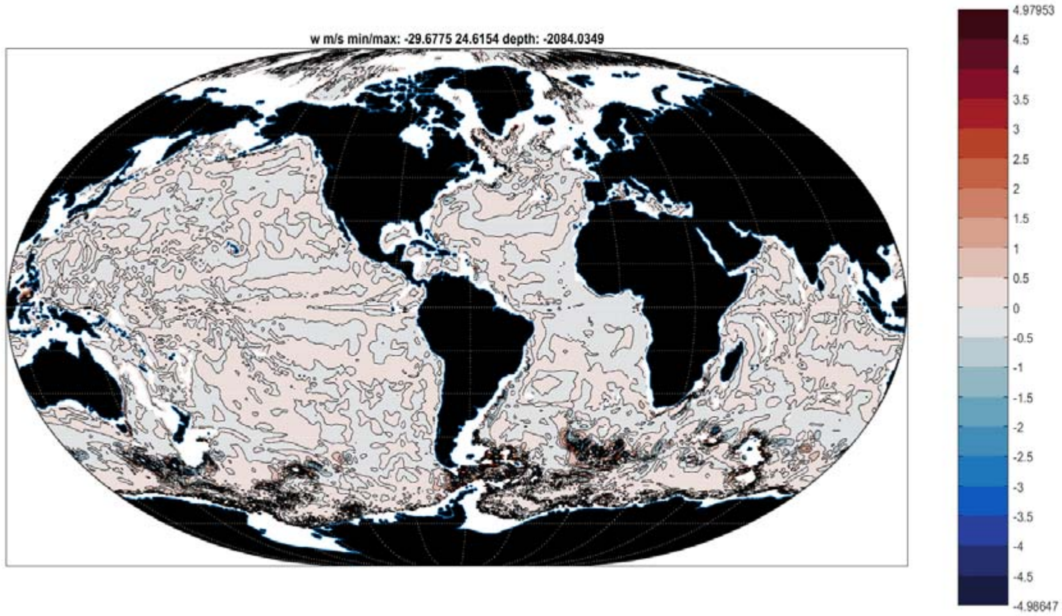


Figure 34: Twenty-year mean Eulerian $w$ at 2100m ($10^5$m/s). At this depth, the complex structures induced by topography come to dominate the patterns. Some extreme values near topographic features have been omitted. See Liang et al. (2017). {map_w_2084m_2

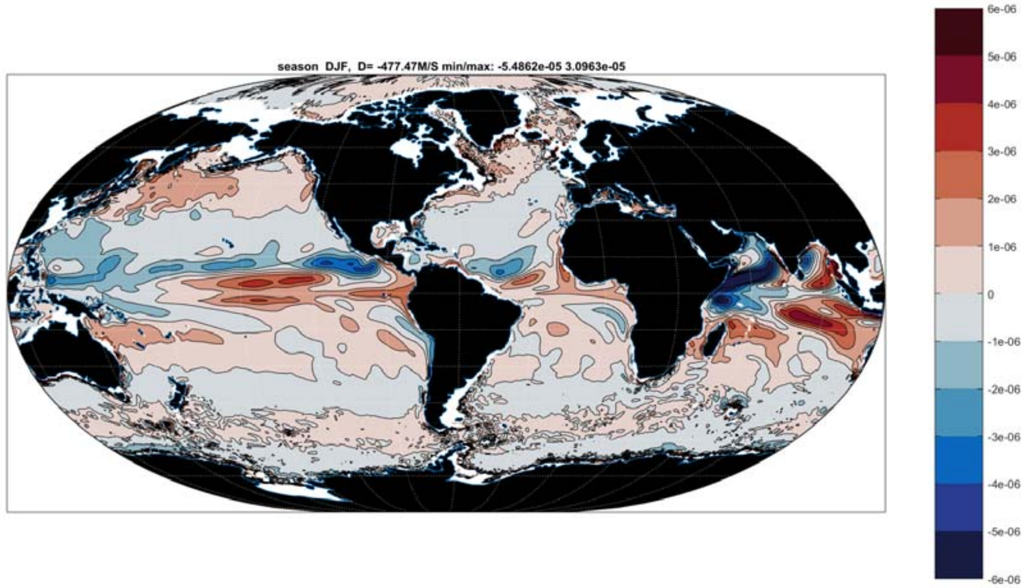


Figure 35: Twenty-year seasonal anomaly of $w$ at 105m DJF.

{mapw_105m_sea

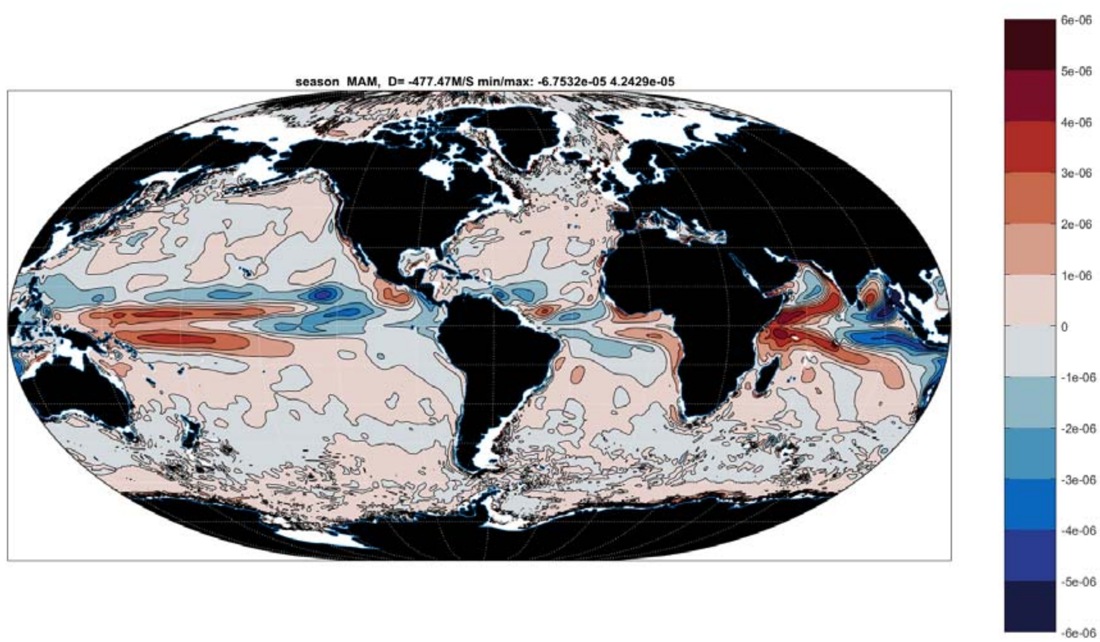


Figure 36: Anomaly of $w$, 105m March, April, May. (m/s, not multiplied by $10^5$)

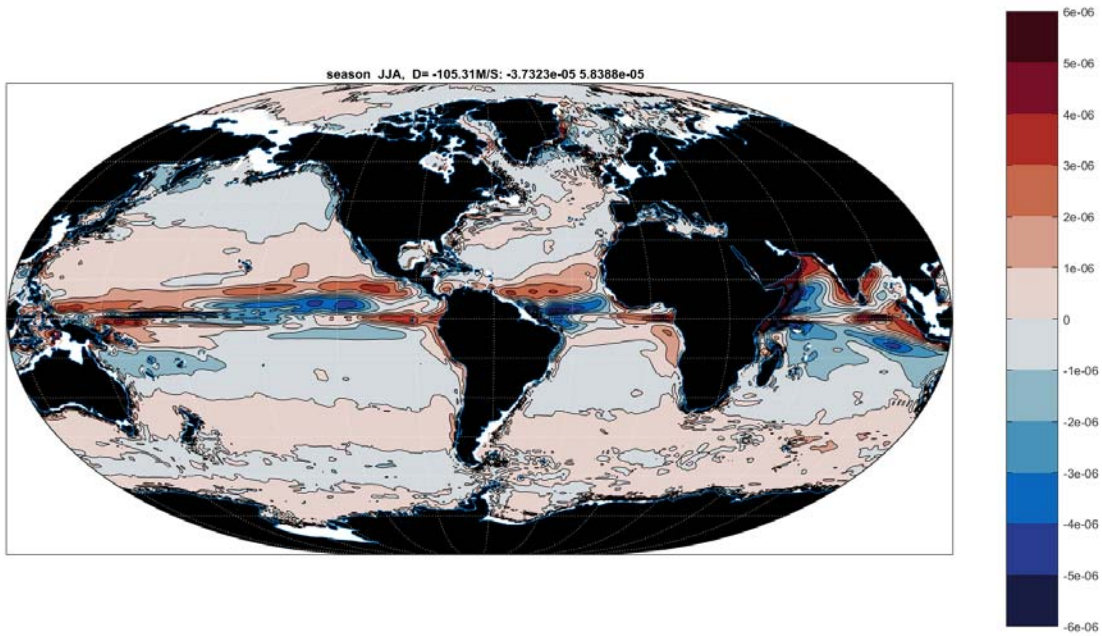


Figure 37: Anomaly of $w$ (m/s) at 105m, June, July, August. {mapw_105m_sea

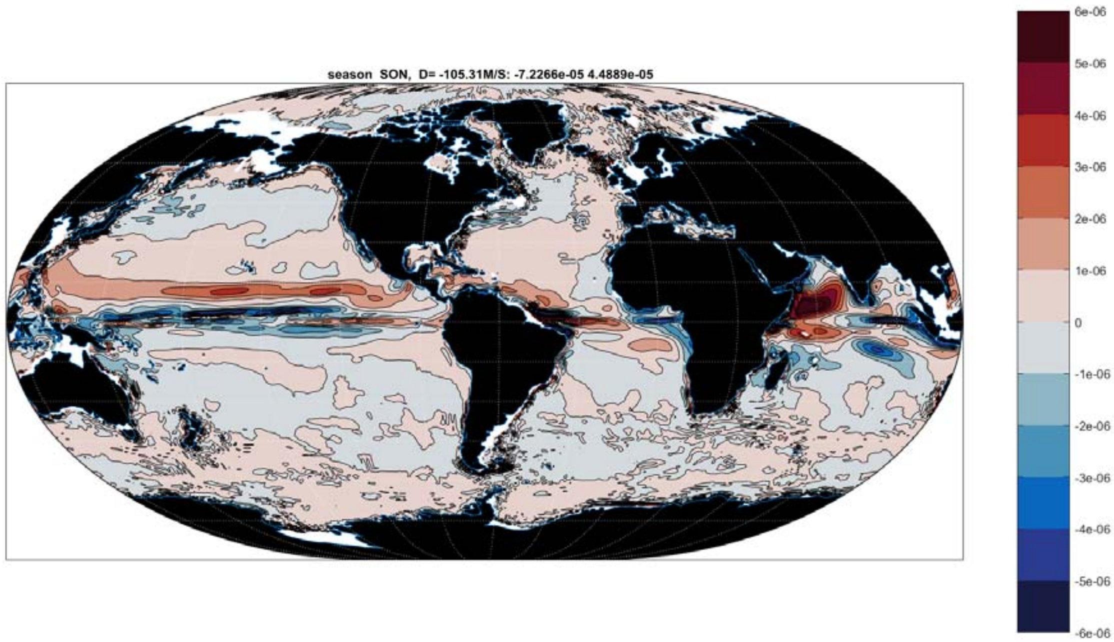


Figure 38: SON anomaly of $w$,105 m (m/s). {mapw_105m_sea

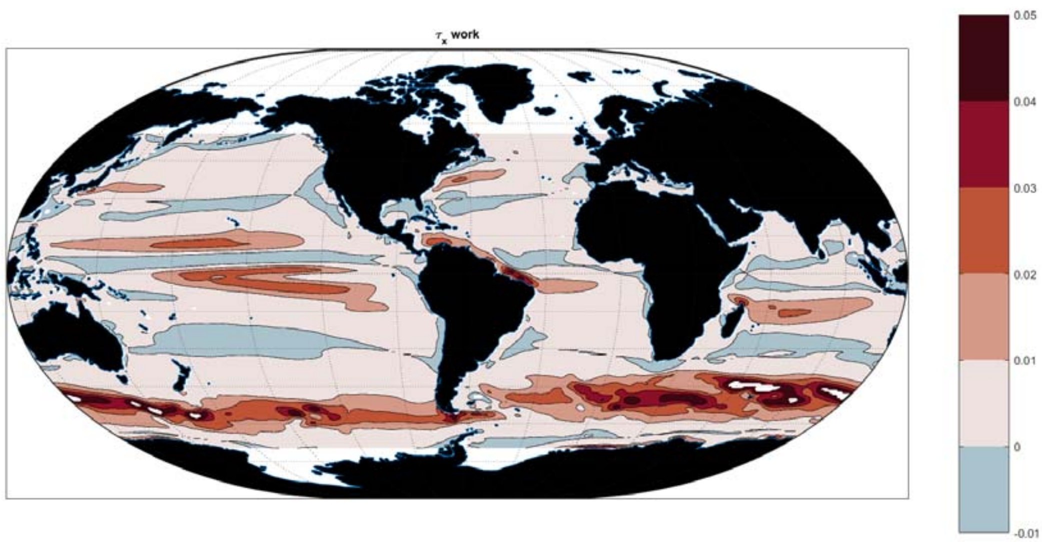


Figure 39: Twenty-year average misfit (here the inferred *correction*) to the time-mean $\tau_x$ (N/m$^2$).The state estimate is obtained by correcting the time-dependent Dee et al. (2014) estimates by a time-varying version of this correction when the model is run forward.

{misfit_taux_m

That reanalysis is not provided with explicit uncertainty estimates, but these have been discussed by Chaudhuri et al. (2014, 2016).

The adjustment (the "misfit" to the reanalysis) to the separate zonal and meridional estimates $(\tau_x, \tau_y)$ are displayed in Figs. 39, **??** for the 20-year average. A generalization is that fitting to oceanic data strengthens both components of $\boldsymbol{\tau}$ at high latitudes, and tends to weaken them in the subtropics and tropics. The global realism of these adjustments remains to be tested. Similar charts can be made for monthly, annual, or seasonal, etc. misfits.

The 20-year average wind-stress as adjusted by the state estimate calculation is shown in Fig. 41. On the large-scale the conventional easterly and westerly wind bands are all prominent. Its curl is shown in Fig. 42 and can be compared to Fig. 32, keeping in mind that the Ekman pumping, $w_E = \nabla \times (\boldsymbol{\tau}/\bar{\rho} f)$.

The rate of wind working on the surface flow (not just the geostrophic component) is readily computed from the products $W_x^{(1)} = \langle \tau_x \rangle \langle u\,(z=5) \rangle\,, W_y^{(1)} \langle \tau_y \rangle \langle v\,(z=5) \rangle$ in Figs. 43, 44 although as discussed earlier, these are only a part of the respective second order products $\langle \tau_x u \rangle$, $\langle \tau_y v \rangle$, and can only be interpreted as the work done by the mean wind on the mean surface flow. Omitting high ice-covered latitudes, thus the spatial average value is $W_x^{(1)} = 0.0043\mathrm{W/m}^2$ and $W_y^{(1)} = -0.00025$ W/m$^2$ which integrate to a total rate of working of about 1.6 TW. Monthly or

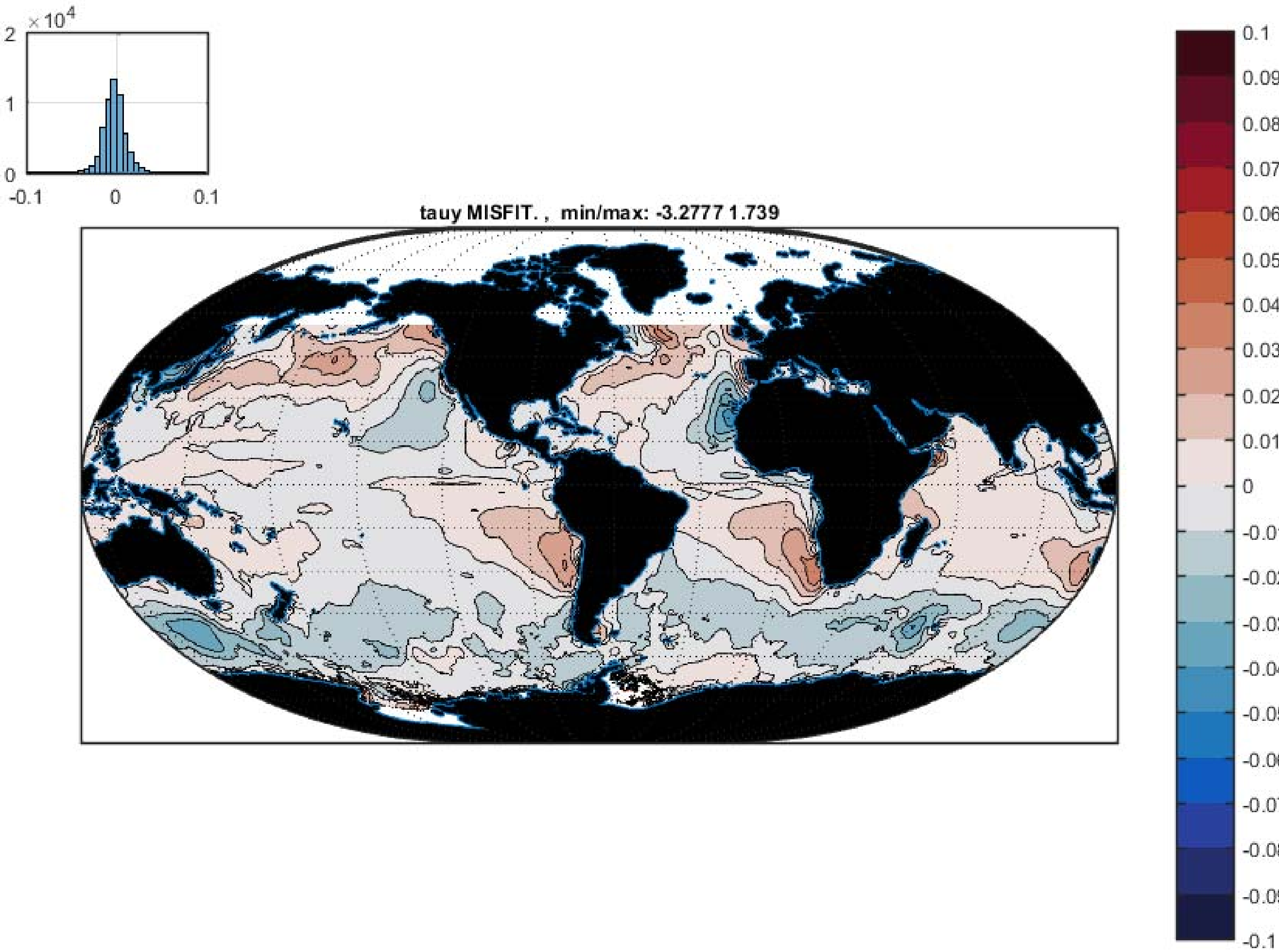


Figure 40: Twenty-year average "misfit" or correction to the time-mean $\tau_y$ (N/m$^2$). {misfit_tauy_2

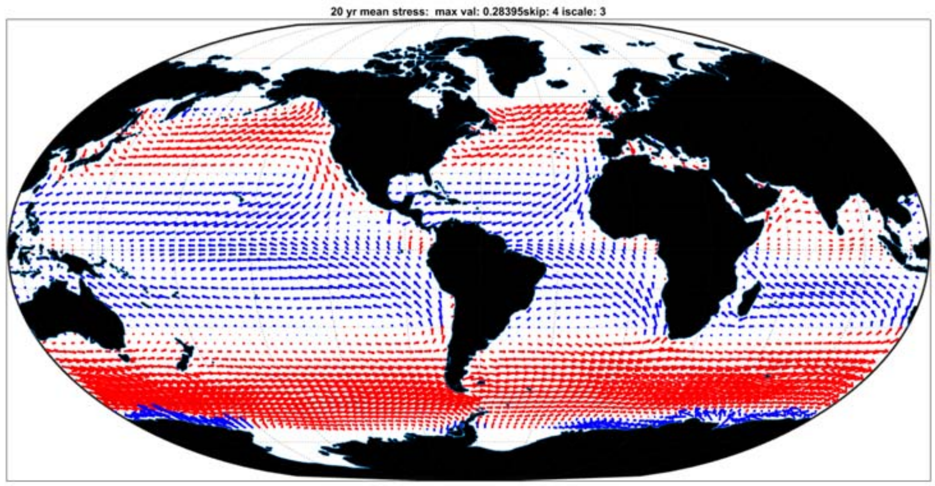


Figure 41: The 20-year average wind stress vectors (N/m$^2$) after adjustment by the state estimate calculation. {quiver_tau_ar

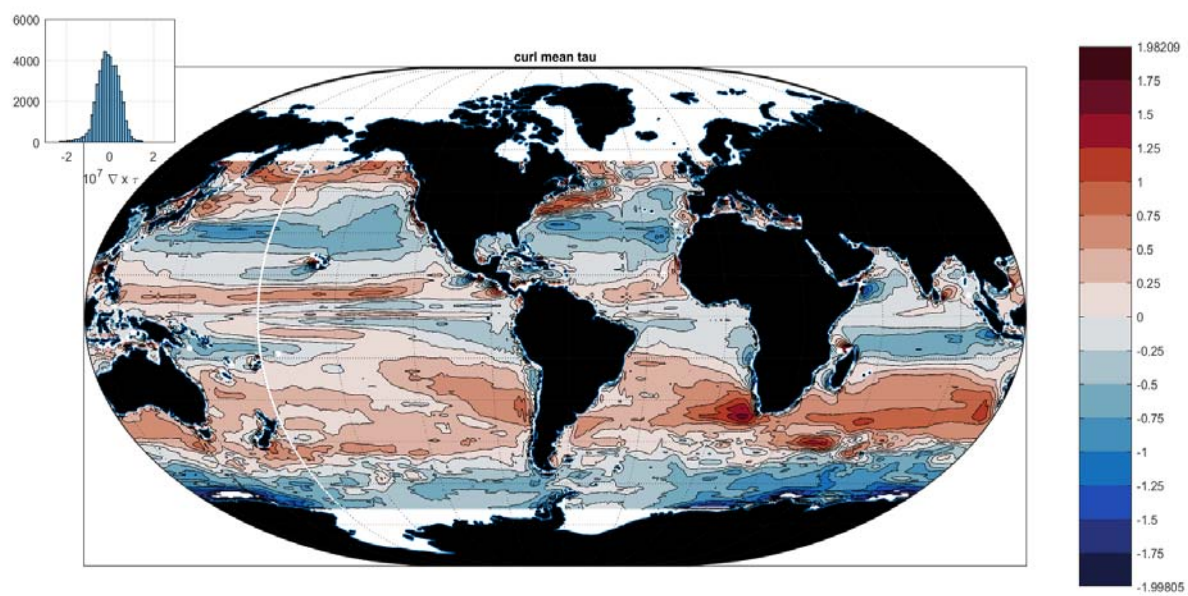


Figure 42: Vertical component of the curl of the 20-year average wind stress in Fig. 41. {curl_20yearme

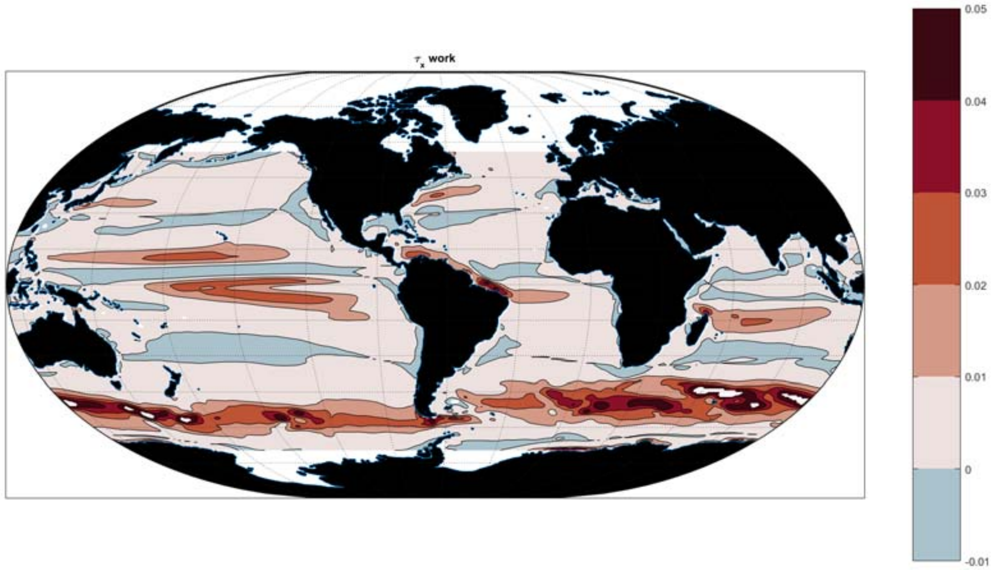


Figure 43: Wind work by the 20-year zonal average wind on the 20-year average surface velocity. (W/m$^2$) {taux_work_map

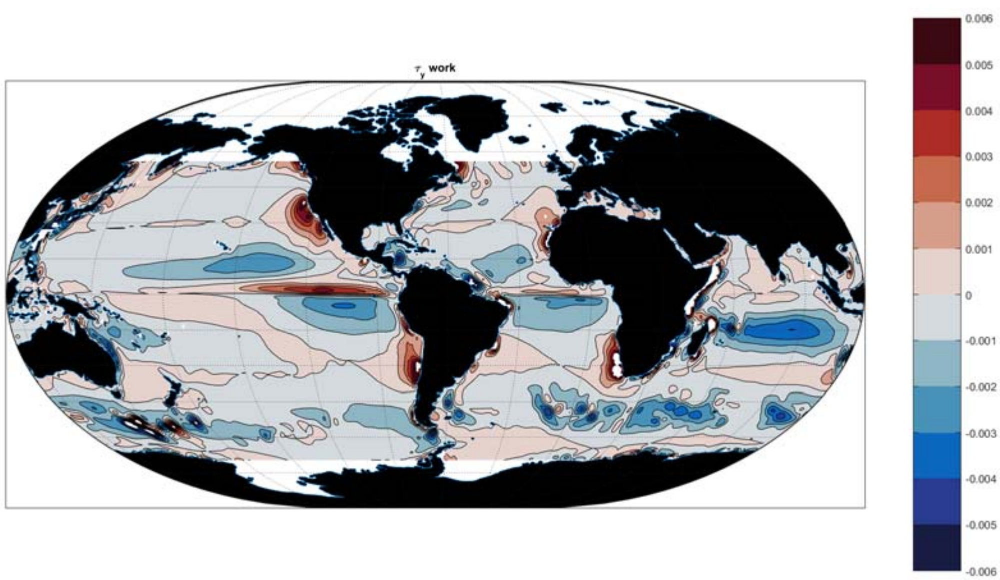


Figure 44: Rate of work on the time-mean sea surface velocity (W/m$^2$) of the meridional component of the wind stress. Note the change in scale from Fig. 43. Coastal upwelling regions tend to dominate. {tauy_work_map

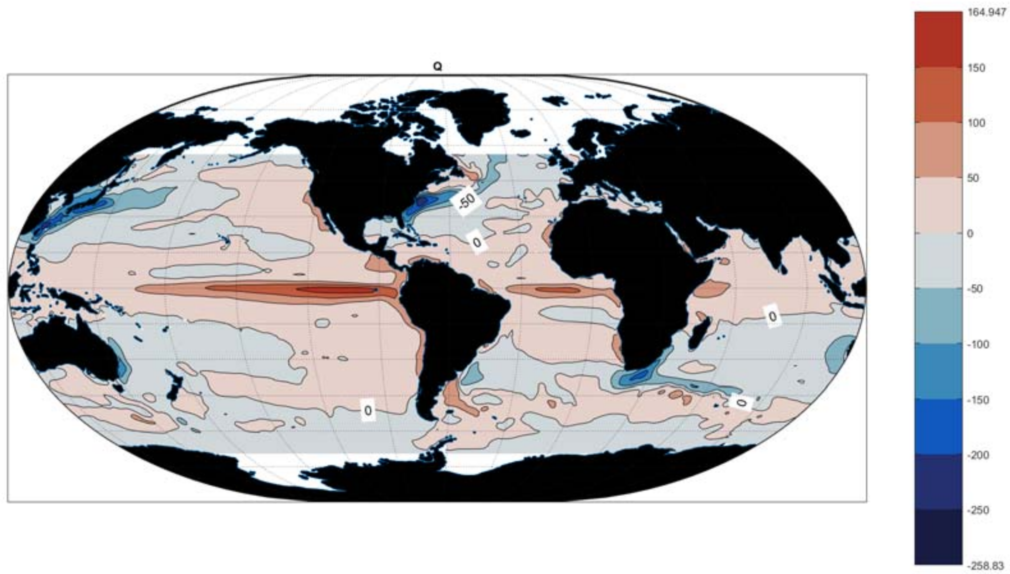


Figure 45: Twenty-year average estimated net heat exchange with the atmosphere (W/m$^2$) with positive values indicating a flux into the ocean.

{q_20yearmean.

seasonal or annual values of the rate of working can readily be computed from the climatology, but pursuit of this subject is left for elsewhere (see Zhai et al., 2012).

*Heat Exchange*

The 20 year average heat exchange, $Q$, with the atmosphere is depicted in Fig. 45 and its 20-year average seasonal anomalies in Fig. 46. Qualitatively, these are all conventional, with heat gain in the tropics and major heat loss over the western boundary currents. Liang and Yu (2016) have compared these and related fields to reanalyses and OAFlux/CERES, showing a greater consistency with observations than do other estimates.

# 6 Eddy Contributions

As described by Forget et al. (2015), the model contains a variety of parameterizations intended to mimic the influence of eddies, waves and a variety of physical processes not properly resolved by the present model grid. Most of these formulas include empirical parameters varying horizontally, with depth, and in some cases, time. A full depiction of all of them would be overwhelming in the present context. As one example of what is now possible, Fig. 47 depicts the so-called bolus velocity at 722m derived from the Gent and McWilliams (1990) parameterization (cf. Ferrari

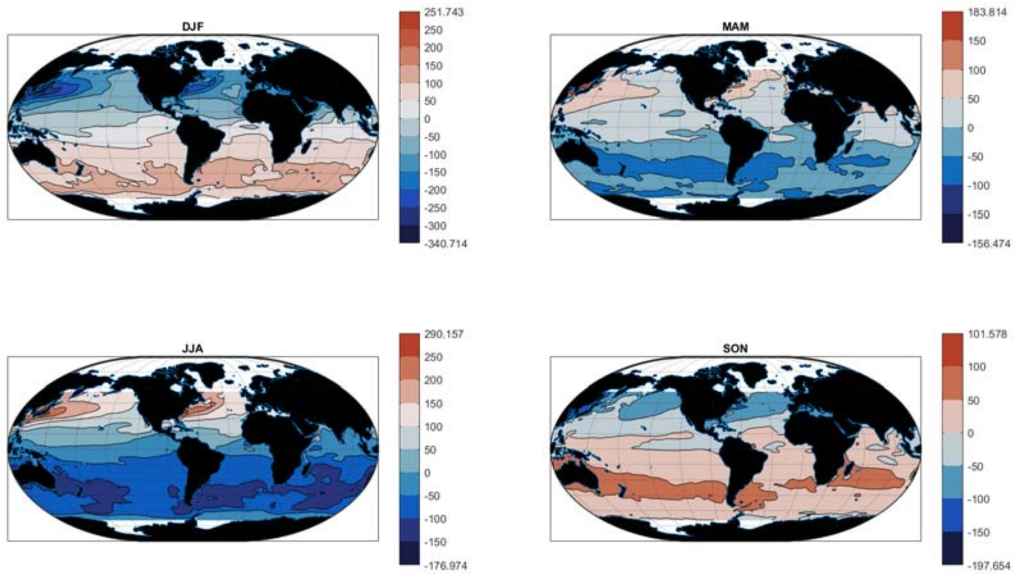


Figure 46: Anomaly of $Q$ (W/m$^2$) by season. Note changes in color scales. {q_anom_4seaso

and Plumb, 2003; Ferreira et al., 2005; Young 2012). As expected, a complex pattern results, one dependent upon the stability properties of the parameterized eddy field. On average, as compared to the Eulerian mean velocities, the relative kinetic energy in the bolus velocities is very small (about 0.5%) of the total. These results too, vary with year, month etc., but are not further displayed here.

*Acknowledgments.* Supported by NASA through the ECCO Consortium through contracts with MIT, AER and JPL.

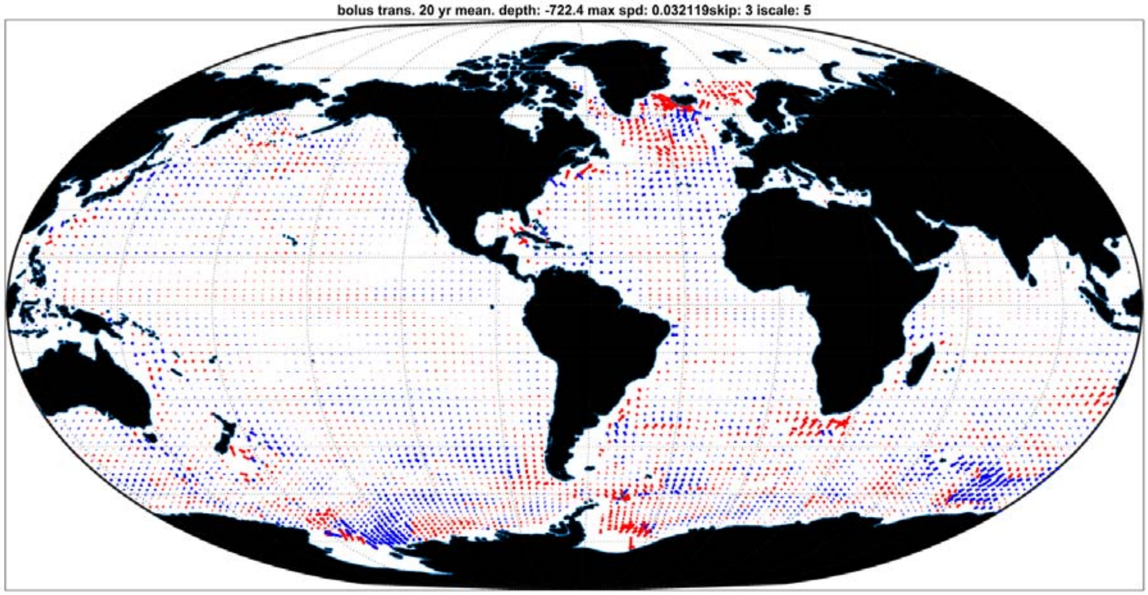


Figure 47: The time mean bolus velocities ($u_{bolus}$,$v_{bolus}$) at 722m (m/s). {quiver_bolus_

# 7 References (Including those from Part 1)

*A full bibliographic list of ECCO publications can be seen at http://ecco-group.org*


Abraham, J. P., Baringer, M., Bindoff, N. L., Boyer, T., Cheng, L. J., Church, J. A.,... Willis, J. K. (2013). A review of global ocean temperature observations" implications for ocean heat content estimates and climate change. Reviews of Geophysics, 51(3), 450-483. doi:10.1002/rog.20022

AchutaRao, K. M., Ishii, M., Santer, B. D., Gleckler, P. J., Taylor, K. E., Barnett, T. P.,... Wigley, T. M. L. (2007). Simulated and observed variability in ocean temperature and heat content. Proceedings of the National Academy of Sciences of the United States of America, 104(26), 10768-10773. doi:10.1073/pnas.0611375104

Adcroft, A., Hill, C., Campin, J. M., Marshall, J., & Heimbach, P. (2004). Overview of the formulation and numerics of the MIT GCM. http://gfdl.noaa.gov/∼aja/papers/ECMWF–2004-Adcroft.pdf

Boyer, T., Domingues, C. M., Good, S. A., Johnson, G. C., Lyman, J. M., Ishii, M.,... Bindoff, N. L. (2016). Sensitivity of global upper-ocean heat content estimates to mapping methods, xbt bias corrections, and baseline climatologies. Journal of Climate, 29(13), 4817-4842. doi:10.1175/JCLI-D-15-0801.1

Bryden, H. L., & Imawaki, S. (2001). Ocean heat transport in, Ocean Circulation and Climate (pp. 455-474): Academic Press, San Diego.

Buckley, M. W., Ponte, R. M., Forget, G., & Heimbach, P. (2014). Low-frequency SST and upper-ocean heat content variability in the North Atlantic. Journal of Climate, 27(13), 4996-5018.

Buckley, M. W., Ponte, R. M., Forget, G., & Heimbach, P. (2015). Determining the origins of advective heat transport convergence variability in the North Atlantic. Journal of Climate, 28(10), 3943-3956.

Chaudhuri, A. H., Ponte, R. M., & Forget, G. (2016). Impact of uncertainties in atmospheric boundary conditions on ocean model solutions. Ocean Modelling, 100, 96-108. doi:10.1016/j.ocemod.2016.02.003

Chaudhuri, A. H., Ponte, R. M., & Nguyen, A. T. (2014). A comparison of atmospheric reanalysis products for the arctic ocean and implications for uncertainties in air-sea fluxes. Journal of Climate, 27(14), 5411-5421. doi:10.1175/jcli-d-13-00424.1

Chelton, D. B., & Schlax, M. G. (1996). Global observations of oceanic Rossby waves. Science, 272(5259), 234-238. doi:10.1126/science.272.5259.234

Colin de Verdière, A., & Ollitrault, M. (2016). A direct determination of the world ocean barotropic circulation. Journal of Physical Oceanography, 46(1), 255-273. doi:10.1175/jpo-d-15-0046.1

Dee, D. P., Balmaseda, M., Balsamo, G., Engelen, R., Simmons, A. J., & Thépaut, J. N. (2014). Toward a Consistent Reanalysis of the Climate System. Bulletin of the American Meteorological Society, 95(8), 1235-1248, doi:10.1175/bams-d-13-00043.1

Dee, D. P., Uppala, S. M. Simmons, A. J., Berrisford, P. et al. (2016) The ERA-Interim reanalysis: configuration and performance of the data assimilation system. Quarterly J. of the Royal Met. Society, 137, 553-597.

Donohue, K. A., Tracey, K. L., Watts, D. R., Chidichimo, M. P., & Chereskin, T. K. (2016). Mean Antarctic Circumpolar Current transport measured in Drake Passage. Geophysical Research Letters, 43(22), 11,760-711,767. doi:10.1002/2016gl070319

Durack, P. J., Wijffels, S. E., & Matear, R. J. (2012). Ocean salinities reveal strong global water cycle intensification during 1950 to 2000. Science, 336(6080), 455-458. doi:10.1126/science.1212222

Elipot, S., Lumpkin, R., Perez, R. C., Lilly, J. M., Early, J. J., & Sykulski, A. M. (2016). A global surface drifter data set at hourly resolution. Journal of Geophysical Research: Oceans.

Evans, D. G., Toole, J., Forget, G., Zika, J. D., Naveira-Garabato, A. C., Nurser, A. J.

G., & Yu, L. Recent wind-driven variability in Atlantic water mass distribution and meridional overturning circulation. Journal of Physical Oceanography, doi:10.1175/jpo-d-16-0089.1

Ferrari, R., & Plumb, R. (2003). Residual circulation in the ocean. Paper presented at the Near-Boundary Processes and Their Parameterization: Proc.'Aha Huliko'a Hawaiian Winter Workshop.

Ferreira, D., Marshall, J., & Heimbach, P. (2005). Estimating eddy stresses by fitting dynamics to observations using a residual-mean ocean circulation model and its adjoint. Journal of Physical Oceanography, 35(10), 1891-1910. doi:10.1175/jpo2785.1

Forget, G. (2010). Mapping ocean observations in a dynamical framework: A 2004-06 ocean atlas. Journal of Physical Oceanography, 40(6), 1201-1221. doi:Doi 10.1175/2009jpo4043.1

Forget, G., Campin, J.-M., Heimbach, P., Hill, C., Ponte, R., & Wunsch, C. (2015). ECCO version 4: an integrated framework for non-linear inverse modeling and global ocean state estimation. Geosci. Model Dev., 8, 3071–3104.

Forget, G., Ferreira, D., & Liang, X. (2015). On the observability of turbulent transport rates by Argo: supporting evidence from an inversion experiment. Ocean Science, 11(5), 839.

Forget, G., & Ponte, R. M. (2015). The partition of regional sea level variability. Progress in Oceanography, 137, 173-195. doi:10.1016/j.pocean.2015.06.002

Forget, G. & Wunsch, C. (2007). Estimated global hydrographic variability. Journal of Physical Oceanography 37, 1997-2008.

Fu, L. L., & Haines, B. J. (2013). The challenges in long-term altimetry calibration for addressing the problem of global sea level change. Advances in Space Research, 51(8), 1284-1300. doi:10.1016/j.asr.2012.06.005

Fuglister, F. C. (1960). Atlantic Ocean Atlas of Temperature and Salinity Profiles and Data from the International Geophysical Year of 1957-1958. Woods Hole Oceanographic Institution.

Fukumori, I., Wang, O., Fenty, I., Forget, G., Heimbach, P.,Ponte, R. (2017) ECCO Version 4 Release 3. Unpublished document. See http://ECCO-group.com

Gebbie, G., Heimbach, P., Wunsch, C. (2006). Strategies for nested and eddy-permitting state estimation. Journal of Geophysical Research-Oceans, 111(C10), Artn C10073. doi 10.1029/2005jc003094

Gent, P. R. & McWilliams, J. C. (1990). Isopycnal mixing in ocean circulation models. Journal of Physical Oceanography, 20, 150-155.

Gill, A. E., & Niiler, P. P. (1973). The theory of the seasonal variability in the ocean. Deep-Sea Res., 20, 141-177.

Gouretski, V. V.,. Koltermann, K. P. (2004). WOCE Global Hydrographic Climatology. Berichte des Bundesamtes für Seeschifffahrt und Hydrographie Nr. 35/2004, Hamburg and Rostock, 50pp.

Griffies, S. M. Danabasoglu, G., Durack, P. J., Adcroft, A. J., et al. (2016). OMIP contribution to CMIP6: Experimental and diagnostic protocol for the physical component of the Ocean Model Intercomparison Project. Geoscientific Model Development, 9, 3231-3296.

Häkkinen, S., Rhines, P. B., & Worthen, D. L. (2013). Northern North Atlantic sea surface height and ocean heat content variability. Journal of Geophysical Research: Oceans, 118(7), 3670-3678. doi:10.1002/jgrc.20268

Hayes, S. P., Mangum, L. J., Picaut, J., Sumi, A., & Takeuchi, K. (1991). TOGA-TAO - a moored array for real-time measurements in the tropical pacific-ocean. Bulletin of the American Meteorological Society, 72(3), 339-347. doi:10.1175/1520-0477(1991)072<0339:ttamaf>2.0.co;2

Ishii, M. Shouji, A., Sugimoto, S., Matsumoto, T. (2005). Objective analyses of sea-surface temperature and marine meteorological variables for the 20th Century using ICOADS and the Kobe Collection. Int'l., J. of Climatology, 25, 865-879.

Kara, A. B., Rochford, P. A., & Hurlburt, H. E. (2003). Mixed layer depth variability over the global ocean. J. Geophys. Res., 108(C3), 3079. doi:10.1029/2000jc000736

Kennedy, J. J., Rayner, N. A., Smith, R. O., Parker, D. E., & Saunby, M. (2011). Reassessing biases and other uncertainties in sea surface temperature observations measured in situ since 1850: 2. Biases and homogenization. Journal of Geophysical Research-Atmospheres, 116. doi:D1410410.1029/2010jd015220

Knudsen, P., & Bingham, R., Andersen, O., Rio, M. H. (2011). A global mean dynamic topography and ocean circulation estimation using a preliminary GOCE gravity model. Journal of Geodesy, 85(11), 861-879. doi:10.1007/s00190-011-0485-8

Koltermann, K. P., Gouretski, V. V., & Jancke, K. (Eds.). (2011). Hydrographic Atlas of the World Ocean Circulation Experiment (WOCE). Volume 3: Atlantic Ocean International WOCE Project Office, Southampton, UK, ISBN 090417557X.

Levitus, S. (1982). Climatological Atlas of the World Ocean. NOAA Professional Paper 13

Liang, X., Piecuch, C. G., Ponte, R. M., Forget, G., Wunsch, C., & Heimbach, P. (2017). Change of the global ocean vertical heat transport over 1993-2010. Submitted for publication.

Liang, X., Wunsch, C., Heimbach, P., & Forget, G. (2015). Vertical redistribution of oceanic heat content. J. Clim., 28, 3821-3833.

Liang, X. F., & Yu, L. (2016). Variations of the global net air-sea heat flux during the "hiatus" period (2001-10). Journal of Climate, 29(10), 3647-3660. doi:10.1175/jcli-d-15-0626.1

Marshall, J., A. Adcroft, C. Hill, L. Perelman, & Heisey, C. (1997). A finite-volume, incompressible Navier Stokes model for studies of the ocean on parallel computers. J. Geophys. Res., 102, 5753-5766.

Maximenko, N., Niiler, P., Rio, M. H., Melnichenko, O., Centurioni, L., Chambers, D.,...

Galperin, B. (2009). Mean dynamic topography of the ocean derived from satellite and drifting buoy data using three different techniques. Journal of Atmospheric and Oceanic Technology, 26(9), 1910-1919. doi:10.1175/2009jtecho672.1

Mazloff, M. R., & Heimbach, P., Wunsch, C. (2010). An eddy-permitting Southern Ocean state estimate. Journal of Physical Oceanography, 40(5), 880-899. doi:Doi 10.1175/2009jpo4236.1

Meredith, M. P., Woodworth, P. L., Chereskin, T. K., Marshall D. P. et al. (2011). Sustained monitoring of the Southern Ocean at Drake Passage: Past achievements and future priorities. Reviews of Geophysics, 49(4), http://doi.org.10.1029/2010RG000348.

Ollitrault, M., & Verdière, A. C. d. (2014). The ocean general circulation near 1000-m depth. Journal of Physical Oceanography, 44(1), 384-409. doi:10.1175/jpo-d-13-030.1

Pavlis, N. K., Holmes, S. A., Kenyon, S. C., & Factor, J. K. (2012). The development and evaluation of the Earth Gravitational Model 2008 (EGM2008). Journal of Geophysical Research-Solid Earth, 117. doi:B04406 10.1029/2011jb008916

Piecuch, C. G., Heimbach, P. Ponte R. M. and Forget, G. L. (2015) Sensitivity of contemporary sea level trends in a global ocean state estimate to effects of geothermal fluxes. Ocean Modelling, 96, 214-220.

Piecuch, C. G., & Ponte, R. M. (2012). Importance of circulation changes to Atlantic heat storage rates on seasonal and interannual time scales. Journal of Climate, 25(1), 350-362. doi:10.1175/jcli-d-11-00123.1

Pillar, H. R., Heimbach, P., Johnson, H. L., & Marshall, D. P. (2016). Dynamical attribution of recent variability in atlantic overturning. Journal of Climate, 29(9), 3339-3352. doi:10.1175/jcli-d-15-0727.1

Ponte, R. M., C. Wunsch, & Stammer, D. (2007). Spatial mapping of time-variable errors in TOPEX/POSEIDON and Jason-1 seasurface height mesurements. J. Atm. Oc. Tech„ 24, 1078-1085.

Purkey, S. G., & Johnson, G. C. (2010). Warming of global abyssal and deep southern ocean waters between the 1990s and 2000s: contributions to global heat and sea level rise budgets. Journal of Climate, 23(23), 6336-6351. doi:10.1175/2010jcli3682.1

Quinn, K. J., & Ponte, R. M. (2008). Estimating weights for the use of time-dependent gravity recovery and climate experiment data in constraining ocean models. Journal of Geophysical Research-Oceans, 113(C12). doi:C12013 10.1029/2008jc004903

Rio, M. H., & Hernandez, F. (2004). A mean dynamic topography computed over the world ocean from altimetry, in situ measurements, and a geoid model. Journal of Geophysical Research-Oceans, 109(C12). doi:C12032

10.1029/2003jc002226

Roquet, F., Wunsch, C., Forget, G., Heimbach, P., Guinet, C., Reverdin, G.,... Fedak, M. A. (2013). Estimates of the Southern Ocean general circulation improved by animal-borne instruments. Geophysical Research Letters, 40(23), 6176-6180. doi:10.1002/2013gl058304

Roquet, F., Wunsch, C., Madec, G. (2011). On the patterns of wind-power input to the ocean circulation. J. of Physical Oceangraphy, 41, 2328-2342.

Schlitzer, R. ( 2017). Ocean Data View, odv.awi.de.

Speer, K., & Forget, G. (2013). Global distribution and formation of mode waters. Ocean Circulation and Climate: a 21st Century Perspective, Ocean Circulation and Climate: a 21st Century Perspective,

pp. 211–226, doi:210.1016/B1978-1010-1012-391851- 391852.300009-X

Stammer, D., Balmaseda, M., Heimbach, P., Köhl, A., & Weaver, A. (2016). Ocean data assimilation in support of climate applications: status and perspectives. Annual Review of Marine Science, 8(1), 491-518. doi:10.1146/annurev-marine-122414-034113

Stammer, D., Ueyoshi, K., Kohl, A., Large, W. G., Josey, S. A., & Wunsch, C. (2004). Estimating air-sea fluxes of heat, freshwater, and momentum through global ocean data assimilation. Journal of Geophysical Research-Oceans, 109(C5). doi:C05023 10.1029/2003jc002082

Stammer, D., Wunsch, C., Giering, R., Eckert, C., Heimbach, P., Marotzke, J.,... Marshall, J. (2002). Global ocean circulation during 1992-1997, estimated from ocean observations and a general circulation model. Journal of Geophysical Research-Oceans, 107(C9), Artn 3118, doi 10.1029/2001jc000888

Stommel, H., & Arons, A. B. (1960). On the abyssal circulation of the world ocean-I. Stationary planetary flow patterns on a sphere. Deep-Sea Res., 6, 140-154.

Talley, L. D., Feely, R. A., Sloyan, B. M., Wanninkhof, R., Baringer, M. O., Bullister, J. L.,... Zhang, J. Z. (2016). Changes in ocean heat, carbon content, and ventilation: a review of the first decade of GO-ship Global Repeat Hydrography. In C. A. Carlson & S. J. Giovannoni (Eds.), Annual Review of Marine Science, 8, 185-215

Thyng, K. M., Greene, C. A., Hetland, R. D., Zimmerle, H. M., DiMarco, S. F. (2016). True colors of oceanography. Guidelines for effective and accurate colormap selectioni. Oceanography, 29(3), 9-13

Vinogradov, S. V., Ponte, R. M., Heimbach, P., & Wunsch, C. (2008). The mean seasonal cycle in sea level estimated from a data-constrained general circulation model. Journal of Geophysical Research-Oceans, 113(C3). doi:C03032

10.1029/2007jc004496

Vinogradova, N. T., & Ponte, R. M. (2016). In search for fingerprints of the recent intensification of the ocean water cycle. J. Clim., in press.

Vinogradova, N. T., Ponte, R. M., Fukumori, I., & Wang, O. (2014). Estimating satellite salinity errors for assimilation of Aquarius and SMOS data into climate models. Journal of Geophysical Research-Oceans, 119(8), 4732-4744, doi:10.1002/2014jc009906

Wunsch, C. (2011). The decadal mean ocean circulation and Sverdrup balance. J. Mar. Res., 69, 417-434.

Wunsch, C. (2015). Modern Observational Physical Oceanography: Princeton Un. Press.

Wunsch, C. (2016). Global Ocean Integrals and Means, with Trend Implications. In C. A. Carlson & S. J. Giovannoni (Eds.), Annual Review of Marine Science, Vol 8 (Vol. 8, pp. 1-+).

Wunsch, C., & Heimbach, P. (2013). Dynamically and kinematically consistent global ocean circulation state estimates with land and sea ice. In J. C. G. Siedler, W. J. Gould, S. M. Griffies, Eds. (Ed.), Ocean Circulation and Climate, 2nd Edition (pp. 553-579): Elsevier.

Wunsch, C., & Heimbach, P. (2014). Bidecadal thermal changes in the abyssal ocean and the observational challenge. J. Phys. Oc., 44, 2013-2030.

Young, W. R. (2012). An exact thickness-weighted average formulation of the Boussinesq equations. Journal of Physical Oceanography, 42(5), 692-707. doi:10.1175/jpo-d-11-0102.1

Zhai, X. M., & Johnson, H. L., Marshall, D. P., Wunsch, C. (2012). On the wind power input to the ocean general circulation. Journal of Physical Oceanography, 42(8), 1357-1365. doi:10.1175/jpo-d-12-09.1